A NEW MULTI-DIMENSIONAL GENERAL RELATIVISTIC NEUTRINO HYDRODYNAMICS CODE OF CORE-COLLAPSE SUPERNOVAE
III. GRAVITATIONAL WAVE SIGNALS FROM SUPERNOVA EXPLOSION MODELS

BERNHARD MÜLLER, HANS-THOMAS JANKA, ANDREAS MAREK
Draft version March 13, 2013

ABSTRACT

We present a detailed theoretical analysis of the gravitational-wave (GW) signal of the post-bounce evolution of core-collapse supernovae (SNe), employing for the first time relativistic, two-dimensional (2D) explosion models with multi-group, three-flavor neutrino transport based on the ray-by-ray-plus approximation. The waveforms reflect the accelerated mass motions associated with the characteristic evolutionary stages that were also identified in previous works: A quasi-periodic modulation by prompt postshock convection is followed by a phase of relative quiescence before growing amplitudes signal violent hydrodynamical activity due to convection and the standing accretion shock instability during the accretion period of the stalled shock. Finally, a high-frequency, low-amplitude variation from proto-neutron star (PNS) convection below the neutrinosphere appears superimposed on the low-frequency trend associated with the aspherical expansion of the SN shock after the onset of the explosion. Relativistic effects in combination with detailed neutrino transport are shown to be essential for quantitative predictions of the GW frequency evolution and energy spectrum, because they determine the structure of the PNS surface layer and its characteristic g-mode frequency. Burst-like high-frequency activity phases, correlated with sudden luminosity increase and spectral hardening of electron (anti-)neutrino emission for some 10 ms, are discovered as new features after the onset of the explosion. They correspond to intermittent episodes of anisotropic accretion by the PNS in the case of fallback SNe. We find stronger signals for more massive progenitors with large accretion rates. The typical frequencies are higher for massive PNSs, though the time-integrated spectrum also strongly depends on the model dynamics.

Subject headings: supernovae: general—neutrinos—radiative transfer—hydrodynamics—gravitation–gravitational waves

1. INTRODUCTION

Core-collapse supernovae have been considered as a source of gravitational waves (GWs) since the 1960s (Weber 1966). While they may have been ousted by compact binary mergers as the most promising source for the first direct detection of GWs by now, the prospective GW signal from a nearby supernova may still provide enormously important clues about the dynamics in the supernova core, shed light on the nature of the explosion mechanism, and could possibly provide constraints for the equation of state (EoS) of neutron star matter. If supernovae are to become a fruitful subject of the future field of observational GW astronomy, this will require reliable waveform predictions, and these can only be based on simulations that accurately capture the evolution from the collapse through several hundreds of milliseconds of accretion by the stalled shock front into the explosion phase – a formidable challenge considering the host of different factors (neutrino transport, multi-dimensional hydrodynamical instabilities, general relativity, EoS physics, etc.) that influence the dynamics.

There is a number of possible scenarios for GW emission from supernovae. *Rotating* progenitors already produce a signal during the phases of collapse and bounce due to the breaking of spherical symmetry, a scenario which has long received interest from the numerical relativity community in particular (see Ott 2009 for an extensive review). State-of-the art predictions of the GW signal come from 2D and 3D general relativistic simulations (Ott et al. 2007a; Dimmelmeier et al. 2007a, 2008; Abdikamalov et al. 2010; Ott et al. 2012) employing a parametrized "deleptonization scheme" for the core-collapse phase (Liebendörfer 2005), and, most recently, a neutrino leakage treatment for the post-bounce phase (Ott et al. 2012). The accuracy of this current approach is yet to be tested against self-consistent models including neutrino transport, but it is conceivable that the dynamics of rotational collapse can be captured reasonably well even with a simplified neutrino treatment. However, the fact that most supernova progenitors are believed to rotate rather slowly (Heger et al. 2005) implies that the signal from rotational core bounce may be weak and difficult to detect.

The situation is different for the GWs produced by the different hydrodynamical instabilities that develop during the post-bounce phase also in non-rotating progenitors, such as convection in the proto-neutron star (as first pointed out by Epstein 1979), in the neutrino-heated hot-bubble region (Bethe 1990; Herant et al. 1992, 1994; Burrows et al. 1995; Janka & Müller 1996; Müller & Janka 1997), the standing accretion-shock instability ("SASI", Blondin et al. 2003; Blondin & Mezzacappa 2006; Foglizzo et al. 2006; Ohnishi et al. 2006; Foglizzo et al. 2007; Scheck et al. 2008; Iwakami et al. 2008, 2009; Fernández & Thompson 2009; Fernández 2010).

Regardless of the actual nature of the explosion mechanism, the evolution during the post-bounce phase depends crucially on the effects of neutrino heating and

cooling and thus requires an elaborate treatment of the microphysics and in particular of the neutrino transport. Because of this constraint, studies addressing the GW signal from the first several hundreds of milliseconds of the post-bounce evolution have been limited either to the Newtonian approximation or the "pseudo-Newtonian effective potential" approach (Marek et al. 2006) until now. Since the 1990s, several authors have investigated the problem in 2D and 3D, mostly relying on parametrized approximations for the neutrino heating and cooling (Müller & Janka 1997; Kotake et al. 2007; Murphy et al. 2009; Kotake et al. 2009), the IDSA method (Scheidegger et al. 2010), or on gray neutrino transport schemes (Fryer et al. 2004; Müller et al. 2012c). In addition, gravitational waveforms from state-of-the art multi-group neutrino hydrodynamics simulations of core-collapse supernovae have become available during the recent years (Müller et al. 2004; Ott et al. 2006; Marek et al. 2009; Yakunin et al. 2010). These different (pseudo-)Newtonian studies have by now established the qualitative features of the GW signal from the post-bounce phase: During the first several tens of milliseconds, prompt post-shock convection gives rise to a quasi-periodic signal in the range around 100 Hz (Marek et al. 2009; Murphy et al. 2009; Yakunin et al. 2010), which is followed by a period of reduced GW activity until hot-bubble convection and the SASI become vigorous and lead to the emission of a stochastic signal with typical frequencies of several hundreds of Hz (Müller et al. 2004; Marek et al. 2009; Murphy et al. 2009). After the onset of the explosion, asymmetric shock expansion may produce a "tail", i.e. a growing offset, in the GW amplitude (Murphy et al. 2009; Yakunin et al. 2010; Müller et al. 2012c), and a high-frequency signal from proto-neutron star convection starts to appear. Tail-like signals may also result from anisotropic neutrino emission (Müller et al. 2004; Marek et al. 2009; Yakunin et al. 2010; Müller et al. 2012c) powered by accretion downflows onto the proto-neutron star.

However, the accuracy of the Newtonian approximation and even of the "effective potential" approach, which have formed the basis of GW predictions for the post-bounce phase so far, is limited. Both 1D studies (Baron et al. 1989; Bruenn et al. 2001; Lentz et al. 2012) as well as the recent 2D models of our own group (Müller et al. 2012b) and exploratory GR simulations with simplified transport in 3D (Kuroda et al. 2012) have demonstrated that GR effects have a non-negligible impact on the neutrino emission, the shock position, and the heating conditions in the supernova core. It is conceivable that GR affects the GW signal to a similar degree. To address this question, we present gravitational waveforms from axisymmetric (2D) general relativistic simulations (using the xCFC approximation of Cordero-Carrión et al. 2009) of the post-bounce phase including multi-group neutrino transport for the first time. We compare our results with predictions from Newtonian and pseudo-Newtonian models. We discuss the relativistic GW signals of six different progenitors with zero-age main sequence masses ranging from $8.1M_\odot$ to $27M_\odot$ (among them five explosion models), part of which have already been studied in Müller et al. (2012b) (paper II) and Müller et al. (2012a). For a $15M_\odot$ star,

two simulations using the Newtonian approximation and the effective potential approach provide the basis for diagnosing GR effects and for working out the reason of systematic differences where possible. We also consider a $15M_\odot$ model with slightly simplified neutrino rates from Müller et al. (2012b). Although the models analyzed in this paper represent the state-of-the-art in 2D core-collapse supernova simulations with energy-dependent neutrino transport, we emphasize that the quest towards better explosion models – ultimately from 3D GR simulations – is continuing apace. For an overview of the current status, the remaining uncertainties of the current generation of models, and future directions in the field the reader should refer to Müller et al. (2012b) as well as recent review articles (Janka 2012; Janka et al. 2012; Kotake et al. 2012; Burrows 2012).

Our paper is structured as follows: In Section 2, we briefly summarize the numerical methods and the model setup, which is laid out in greater detail in Müller et al. (2010, 2012b, paper I and II). In Section 3, we describe the methods used for extracting and analyzing the gravitational wave signals. The wave signals produced during the different phases of the post-bounce evolution – the early phase of shock propagation and prompt post-shock convection, the steady-state accretion phase, and the explosion phase – are discussed in Section 4 on the basis of two exemplary explosion models. The dependence of the gravitational wave emission on the progenitor model is discussed separately in Section 5. Finally, we summarize the most salient features of our relativistic waveforms in Section 6. Important technical issues relied upon in our paper, such as the derivation of a modified GW quadrupole formula, analytic expressions for the GW signal produced by an aspherical shock front, and the Brunt-Väisälä (buoyancy) frequency in GR are treated in Appendices A, B and C. Note that different from the rest of the paper we use geometrical units ($c = G = 1$) in the Appendix.

2. NUMERICAL METHODS AND MODEL SETUP

We analyze the GW emission for several 2D simulations performed with the general relativistic neutrino hydrodynamics code VERTEX-COCONUT (Müller et al. 2010) or its (pseudo)-Newtonian counterpart VERTEX-PROMETHEUS (Rampp & Janka 2002; Buras et al. 2006). The reader should refer to these papers for an in-depth description of the numerical methods and the input physics (including the choice of progenitor models, neutrino interaction rates, and the equation of state). At this point, we confine ourselves to a summary of those technical aspects that are directly relevant for the present paper with its focus on GW signals.

The hydrodynamics modules COCONUT and PROMETHEUS used in conjunction with the neutrino transport solver VERTEX both rely on similar higher-order finite-volume techniques, but differ in their treatment of general relativity. PROMETHEUS solves the equation of Newtonian hydrodynamics, but can optionally account for some effects of strong-field gravity by means of a modified gravitational potential ("effective potential"; Rampp & Janka 2002; Marek et al. 2006). By contrast, the general relativistic equations of hydrodynamics are solved in COCONUT (Dimmelmeier et al. 2002a, 2005), and the extended conformal flatness
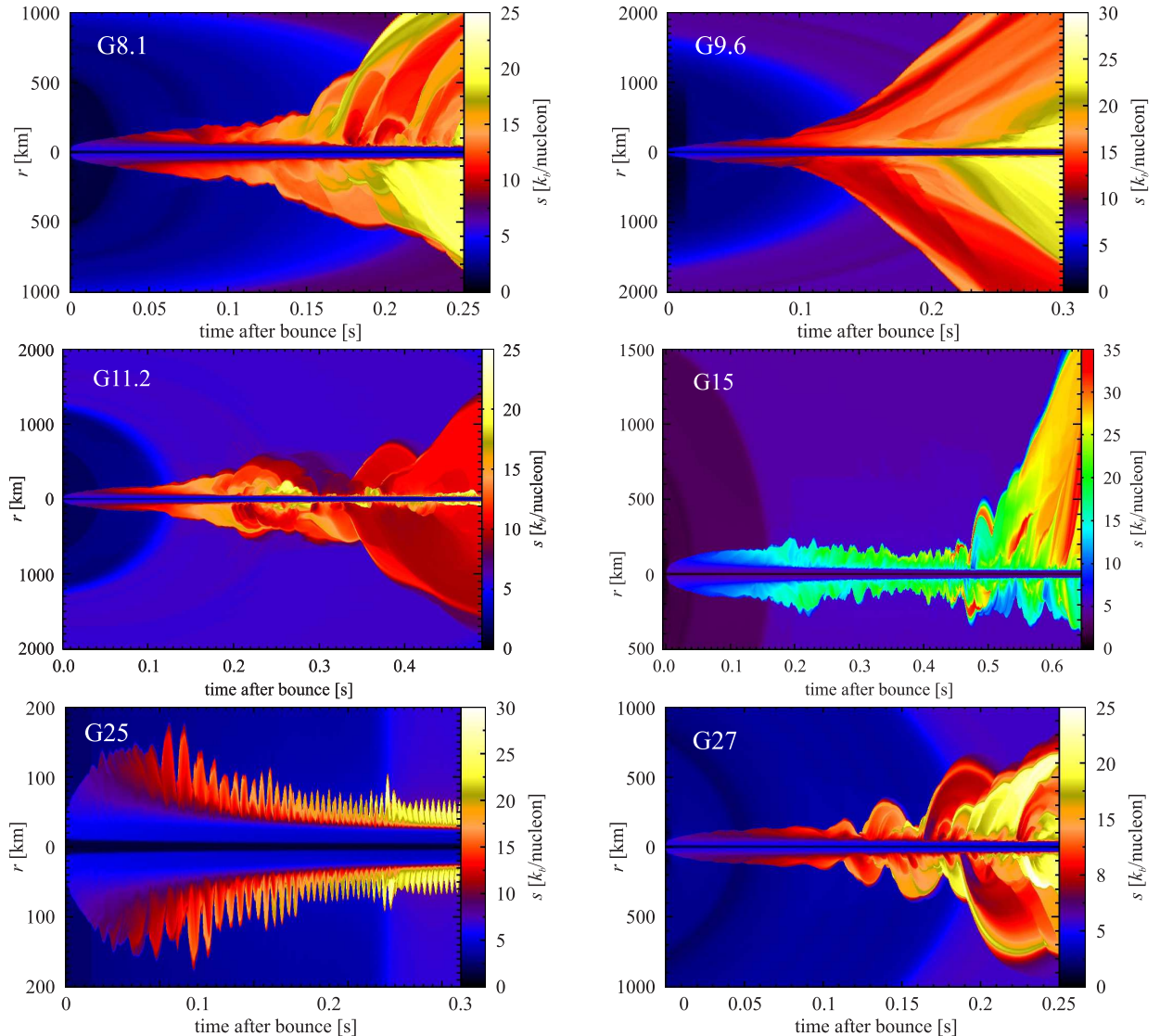
Figure 1. Entropy along the north and south polar axis as a function of time for the relativistic simulations G8.1, G9.6, G11.2, G15, G25, and G27 (top left to bottom right). The shock trajectory is visible as a discontinuity between the darker violet and blue tones in the pre-shock region and lighter colors (red, green, yellow) in the post-shock region.

approximation (xCFC, Cordero-Carrión et al. 2009) is used for the space-time metric. Comparisons of xCFC with the full ADM formalism in the context of rotational core-collapse have shown excellent agreement (Ott et al. 2007a,b; Dimmelmeier et al. 2007b) and suggest that it is fully adequate for capturing the dynamics in the supernova core. However, xCFC is a waveless approximation so that we need to extract the GW signal in a post-processing step with the help of a suitable version of the quadrupole formula (see Section 3).

The neutrino transport module VERTEX solves the energy-dependent neutrino moment equations for all neutrino flavors using a variable Eddington factor technique (Rampp & Janka 2002) and relies on the so-called "ray-by-ray-plus" approximation for multi-dimensional neutrino transport (Buras et al. 2006). The ray-by-ray-plus approach allows us to predict angular variations in the neutrino radiation field (and hence the low-frequency GW signal generated by the neutrinos) at least in rough qualitative agreement with full multi-angle transport

(Ott et al. 2008; Brandt et al. 2011).

In total, we simulate the evolution of six different progenitor models with zero-age main sequence masses ranging from $8.1 M_\odot$ to $27 M_\odot$ (simulations G8.1–G27). These include a metal-poor $8.1 M_\odot$ (10^{-4} solar metallicity) progenitor (model u8.1 in Müller et al. 2012a), and a metal-free $9.6 M_\odot$ star (z9.6, Alexander Heger, private communication), while the other progenitors (models s11.2, s25.0 and s27.0 of Woosley et al. 2002 and model s15s7b2 of Woosley & Weaver 1995) have solar metallicity. Three of the progenitors (z9.6, s25.0, s27.0) were simulated using the equation of state of Lattimer & Swesty (1991) with a bulk incompressibility modulus of nuclear matter of $K = 220$ MeV (LS220), whereas $K = 180$ MeV (LS180) was applied in all other cases. Because of very similar proto-neutron star radii for the neutron star masses encountered in this study, LS220 and LS180 yield very similar results, and the use of LS180 for some of the progenitors is justified despite its marginal inconsistency with the $1.97 M_\odot$ pulsar (Demorest et al. 2010).

Dynamical 1D simulations for the two EoSs with VER-TEX show a very similar evolution of the shock and proto-neutron star radius as well as the neutrino luminosities and mean energies (L. Hüdepohl, private communication), a finding that is in agreement with 1D results of Swesty et al. (1994), Thompson et al. (2003), and of Suwa et al. (2012), who have also found an extremely similar behavior also in 2D.

The general features of the gravitational wave signal from the post-bounce accretion and explosion phases are discussed on the basis of the $11.2M_\odot$ progenitor of Woosley et al. (2002) and the $15M_\odot$ model s15s7b2 of Woosley & Weaver (1995) as prototypes for "early" and "late" explosions. For the $15M_\odot$ progenitor, we also consider three models with a different treatment of gravity (G15: GR; M15: effective potential; N15: purely Newtonian), as well as a GR model (S15) with simplified neutrino rates in order to explore the impact of these factors on the GW signal. The simplifications in model S15 include the use of the FFN rates (Fuller et al. 1982; Bruenn 1985) for electron captures on nuclei, a simpler treatment of neutrino-nucleon reactions, and the omission of neutrino-neutrino pair conversion (see paper II for details).

Except for the $25M_\odot$ case, explosions have been obtained for all progenitors with GR and with the full set of neutrino rates. Figure 1 provides a compact overview over the relativistic (G-)series of simulations: Models G8.1 and G9.6 explode rather early and exhibit convective activity only on a moderate level after the onset of the explosion. The $11.2M_\odot$ model G11.2 shows a much slower expansion of the shock and several violent shock oscillations before the explosion takes off. Model G15 develops a very asymmetric explosion as late as ~ 450 ms. The more massive $25M_\odot$ and $27M_\odot$ models G25 and G27 differ from the other models by a more clearly discernible SASI activity, visible as strong periodic sloshing motions of the shock in Figure 1, which lead to an explosion in the case of G27. We note that no explosion develops in the simulations without GR and/or the full neutrino rates (M15, N15, S15).

A summary of all nine models considered in this paper is given in Table 1. For a detailed discussion of models G11.2 and G15, see Müller et al. (2012b), and for details on G8.1 and G27, see Müller et al. (2012a).

3. GRAVITATIONAL WAVE EXTRACTION

The xCFC approximation used in VERTEX-CoCoNuT does not allow for a direct calculation of gravitational waves as the corresponding degrees of freedom in the metric are missing. We therefore need to extract gravitational waves in a post-processing step with the help of some variant of the Einstein quadrupole formula (Einstein 1918). Modified versions of the Newtonian quadrupole formula (exploiting ambiguities concerning the identification of Newtonian and relativistic hydrodynamical variables) have been found to be reasonably accurate even in the strong-field regime (Shibata & Sekiguchi 2003; Nagar et al. 2007; Cordero-Carrión et al. 2012). For the gauge used in VERTEX-CoCoNuT and the typical conditions in a supernova core, it is possible to derive a modified version of the time-integrated Newtonian quadrupole formula (Finn 1989; Finn & Evans 1990; Blanchet et al. 1990)

directly from the field equations (see Appendix A). Assuming axisymmetry, we obtain the quadrupole amplitude A_{20}^{E2} in non-geometrized units for spherical polar coordinates as

$$A_{20}^{\mathrm{E2}} = \frac{32\pi^{3/2}G}{\sqrt{15}c^4} \int \mathrm{d}\theta\,\mathrm{d}r\phi^6 r^3 \sin\theta \tag{1}$$

$$\left\{ \frac{\partial}{\partial t} \left[S_r \left(3\cos^2\theta - 1 \right) + 3r^{-1}S_\theta \sin\theta\cos\theta \right] \right.$$

$$\left. - \left[\dot{S}_{r,\nu}, \left(3\cos^2\theta - 1 \right) + 3r^{-1}\dot{S}_{\theta,\nu} \sin\theta\cos\theta \right] \right\}.$$

Here, ϕ is the (dimensionless) conformal factor for the three-metric in the CFC spacetime, and S_i denotes the covariant components of the relativistic three-momentum density (in non-geometrical units, i.e. S_r is given in g cm^{-2} s^{-1} and S_θ in g cm^{-1} s^{-1}) in the $3+1$ formalism, which is given in terms of the rest-mass density ρ, the specific internal energy ϵ, the pressure P, the Lorentz factor W, and the covariant three-velocity components v_i as

$$S_i = \rho(1 + \epsilon/c^2 + P/\rho c^2)W^2 v_i. \tag{2}$$

$\dot{S}_{i,\nu}$ denotes the momentum source term for S_i due to neutrino interactions (which must be subtracted from $\partial S_i/\partial t$ as explained in Appendix A). In practice, these neutrino source terms do not yield a significant contribution to the integral in Equation (1).

A_{20}^{E2} determines the dimensionless strain measured by an observer at a distance R and at an inclination angle Θ with respect to the z-axis (see, e.g., Müller 1998),

$$h = \frac{1}{8}\sqrt{\frac{15}{\pi}} \sin^2\Theta \frac{A_{20}^{\mathrm{E2}}}{R}. \tag{3}$$

In the following, we will always assume the most optimistic case of an observer located in the equatorial plane, i.e. $\sin^2\Theta = 1$. In addition to the gravitational wave signal from the matter, we compute the gravitational wave signal due to anisotropic neutrino emission using the Epstein formula (Epstein 1978; Müller & Janka 1997) for the gravitational wave strain h_ν,

$$h_\nu = \frac{2G}{c^4 R} \int_0^t L_\nu(t')\alpha_\nu(t')\,\mathrm{d}t'. \tag{4}$$

Here L_ν is the total angle-integrated neutrino energy flux, and the anisotropy parameter α_ν can be obtained as

$$\alpha_\nu = \frac{1}{L_\nu} \int \pi \sin\theta \left(2|\cos\theta| - 1\right) \frac{\mathrm{d}L_\nu}{\mathrm{d}\Omega}\mathrm{d}\Omega \tag{5}$$

in axisymmetry (Kotake et al. 2007). h_ν can be converted into an amplitude $A_{20,\nu}^{\mathrm{E2}}$ by inverting Equation (3).

The energy E_{GW} radiated in gravitational waves can be computed from $A_{20,\nu}^{\mathrm{E2}}$ as follows (see, e.g., Müller 1998),

$$E_{\mathrm{GW}} = \frac{c^3}{32\pi G} \int \left(\frac{\mathrm{d}A_{20,\nu}^{\mathrm{E2}}}{\mathrm{d}t} \right)^2 \mathrm{d}t. \tag{6}$$

We also calculate the spectral energy distribution $\mathrm{d}E/\mathrm{d}f$ of the gravitational waves,

$$\frac{\mathrm{d}E}{\mathrm{d}f} = \frac{c^3}{16\pi G} (2\pi f)^2 \left| \int_{-\infty}^{\infty} e^{-2\pi i f t} A_{20}^{\mathrm{E2}}(t)\,\mathrm{d}t \right|^2. \tag{7}$$

Table 1
Model setup

model	progenitor	neutrino opacities	treatment of relativity	simulated post-bounce time	angular resolution	explosion obtained	time of explosion[a]	EoS
G8.1	u8.1	full set	GR hydro + xCFC	325 ms	1.4°	yes	175 ms	LS180
G9.6	z9.6	full set	GR hydro + xCFC	735 ms	1.4°	yes	125 ms	LS220
G11.2	s11.2	full set	GR hydro + xCFC	950 ms	2.8°	yes	213 ms	LS180
G15	s15s7b2	full set	GR hydro + xCFC	775 ms	2.8°	yes	569 ms	LS180
S15	s15s7b2	reduced set	GR hydro + xCFC	474 ms	2.8°	no	—	LS180
M15	s15s7b2	full set	Newtonian + modified potential	517 ms	2.8°	no	—	LS180
N15	s15s7b2	full set	Newtonian (purely)	525 ms	1.4°	no	—	LS180
G25	s25.0	full set	GR hydro + xCFC	440 ms	1.4°	no	—	LS220
G27	s27.0	full set	GR hydro + xCFC	765 ms	1.4°	yes	209 ms	LS220

[a]Defined as the point in time when the average shock radius $\langle r_{\rm sh} \rangle$ reaches 400 km.

Previous studies (Marek et al. 2009; Murphy et al. 2009; Müller et al. 2012c) have relied on Fourier transform methods (such as the short-time Fourier transform) for analyzing temporal variations in the frequency structure of the signal. While the Fourier transform of the signal can be related directly to the power radiated in gravitational waves, the time-variable frequency structure of the signal can be captured more sharply with wavelet transforms.

We therefore compute the wavelet transform $\chi(t, f)$ (expressed as a function of time and frequency) of the gravitational wave signal using the Morlet wavelet (see, e.g., Equations 1 and 2 and Table 1 of Torrence & Compo 1998) with wavenumber $k = 20$ and define a normalized power spectrum $\bar{\chi}(t, f)$:

$$\bar{\chi}(t, f) = \frac{f \, |\chi(t, f)|^2}{\max\limits_{f' \in \mathbb{R}^+} \left(f' \, |\chi(t' = t, f')|^2 \right)}. \qquad (8)$$

In other words: At a given time t, $\bar{\chi}$ is obtained by dividing the weighted wavelet transform $f \, |\chi(t, f)|^2$ by its maximum over all frequencies for that time slice. The frequency weighting has been chosen in correspondence with the energy spectrum in Equation (7).[1] We found that this weighting and normalization procedure helps to reveal the frequency structure of the signal most perspicuously.

## 4. EXEMPLARY DISCUSSION OF GW SIGNAL FEATURES FOR $11.2 M_\odot$ AND $15 M_\odot$ MODELS

4.1. *Qualitative Description of the GW Signal*

GW amplitudes (both for the matter and neutrino signals) for models G11.2, G15, M15, N15, and S15 are given in the left panels of Figures 2–6, and the evolution of the signal in frequency space is illustrated with the help of wavelet spectra in the right panels of these Figures. Qualitatively, our gravitational waveforms share almost all the characteristics of waveforms recently obtained from (pseudo-)Newtonian simulations of core-collapse supernova explosions (Marek et al. 2009; Murphy et al. 2009; Yakunin et al. 2010): We observe a

---

[1] A weighting factor f instead of f^2 is used because of the usual scale-dependent (i.e. frequency-dependent) normalization of the wavelet transform.

quasi-periodic signal during the phase of prompt post-shock convection roughly between 10 ms and $50 - 70$ ms after bounce, which is followed by a more quiescent phase of several tens of milliseconds until hot-bubble convection and increased SASI activity set in and produce a strong stochastic signal component. The stochastic signal in Figure 2 is strongest during the first 200 ms after the onset of the explosion, and then continues at a lower amplitude with proto-neutron star convection taking over as the dominant source for high-frequency gravitational waves. Model G15 (Figure 3) also shows a "tail" with a steadily increasing wave amplitude in the explosion phase, a feature which is due to the expansion of a strongly prolate shock as recognized by Murphy et al. (2009) and Yakunin et al. (2010). In addition, anisotropic neutrino emission gives rises to an almost monotonically growing amplitude from about 200 ms onward, which is, in fact, much larger than the "tail" in the matter signal. Model G11.2, on the other hand, exhibits a new feature: Here we observe several bursts of high-frequency gravitational wave emission in the explosion phase with amplitudes comparable to the phase of hot-bubble convection – a phenomenon that turns out to be connected to the fallback of material onto the proto-neutron star in a rather weak explosion (Müller et al. 2012b).

The wavelet spectra in Figures 2–6 equally reflect the evolution through these different phases. The early quasi-periodic signal initially produces a peak at $\sim$ 100 Hz, which is clearly discernible during the first $\sim$ 100 ms. During the subsequent phase of reduced gravitational wave activity, there is no clearly identifiable narrow emission band, instead broadband low-frequency (model G11.2 until $\sim$ 200 ms) or high-frequency (model G15 around $\sim$ 150 ms) noise dominates the spectrum. For models M15, N15, and S15 this intermediate phase is not very pronounced in the wavelet spectra. The subsequent phase of strong SASI activity and hot-bubble convection is mostly characterized by a relatively narrow emission band, which appears between 100 ms and 200 ms (depending on the simulation) and gradually shifts to higher frequencies at later times. Except for model N15, there is also considerable gravitational wave activity at frequencies above this band. This contribution disappears in the later explosion phase ($\gtrsim$ 600 ms), leaving a single, relatively sharply defined
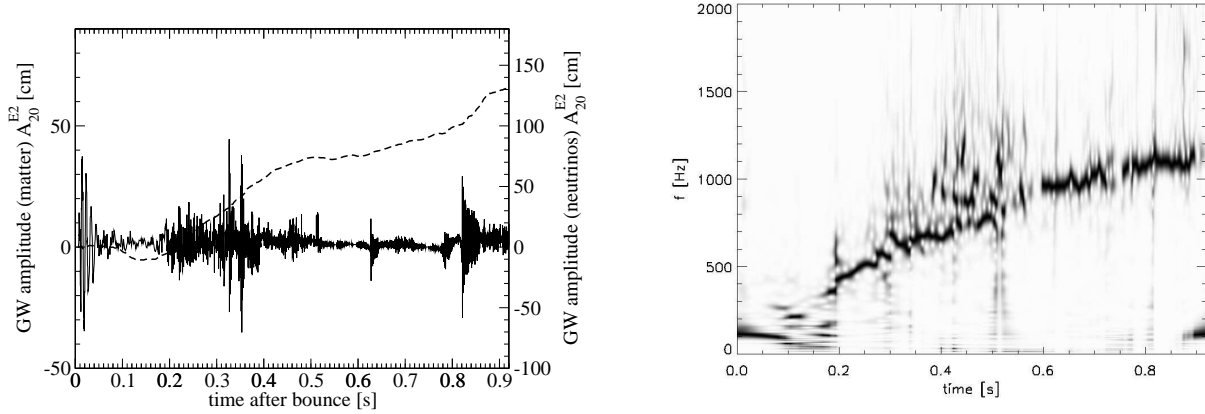
Figure 2. Left panel: Matter (solid lines) and neutrino (dashed lines) gravitational wave signals for model G11.2. Note that the scale for the matter signal (left vertical axis) is different from the scale for the neutrino signal (right vertical axis). Right panel: Normalized wavelet spectrum $\bar{\chi}(t, f)$ of the matter signal for model G11.2. The grayscale ranges from white ($\bar{\chi} = 0$) to black ($\bar{\chi} = 1$, maximum value). For the definition of $\bar{\chi}(t, f)$, see Equation (8).
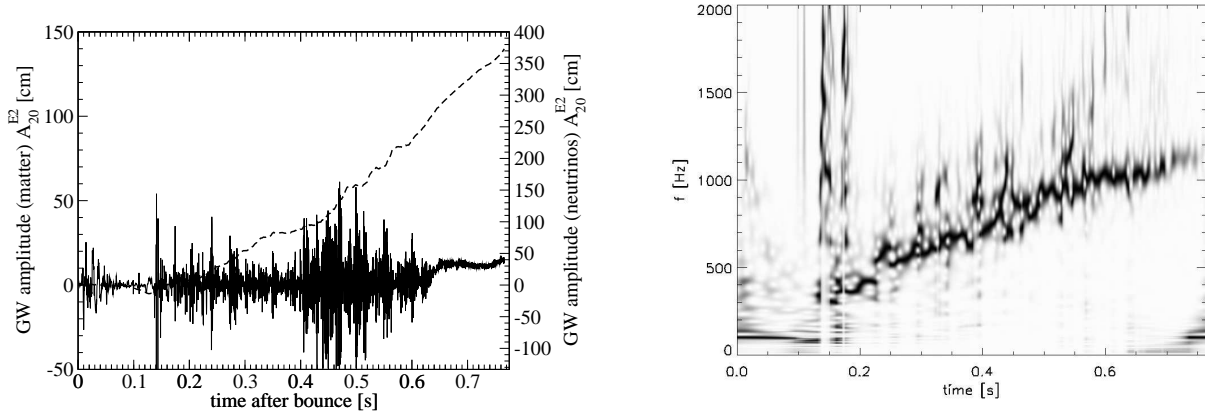
Figure 3. Left panel: Matter (solid lines) and neutrino (dashed lines) gravitational wave signals for model G15. Note that the scale for the matter signal (left vertical axis) is different from the scale for the neutrino signal (right vertical axis). Right panel: Normalized wavelet spectrum $\bar{\chi}(t, f)$ of the matter signal for model G15.

peak frequency. Note that low-frequency components (i.e. asymmetric shock expansion) are poorly reflected in the wavelet spectrum due to their small weighting factor (see Equation (7)).

In the following, we shall discuss specific features of the individual phases of gravitational wave emission in our simulations and study the quantitative impact of GR on the GW signal in more detail. A cursory glance at Figures 2–6 already reveals that the spectra contain "cleaner" information about the specific signal properties of the different models than the stochastically varying amplitudes, but we will nonetheless examine the signals extensively both in the time and in the frequency domain.

4.2. *Early Quasi-periodic Signal*

With regard to the early quasi-periodic signal, two major questions ought to be addressed, namely whether GR affects the typical amplitude and frequency of this signal component, and, even more basically, what is the hydrodynamical origin of the GW signal during this phase? Different authors have ascribed the quasi-periodic signal during the first several tens of milliseconds directly to prompt post-shock convective overturn (Marek et al.

2009; Murphy et al. 2009), while others (Yakunin et al. 2010) have emphasized the contribution of early SASI motions. Yakunin et al. (2010), in particular, argued that the quasi-periodic signal is largely due to the deceleration of the infalling matter at an oscillating aspherical shock.

4.2.1. *Origin of the Signal*

For our simulations, the question about the origin of the "prompt convection" signal can be answered relatively clearly. The deceleration of matter at the shock can be ruled out as major contribution factor with the help of an analytic estimate of the expected (matter) gravitational wave amplitude $A_{20,\mathrm{shock}}^{\mathrm{E2}}$ from a nonstationary aspherical shock wave. For weak SASI oscillations, we obtain the following formula in terms of the pre-shock density ρ_{p}, the ratio of the post-shock and pre-shock densities β, the power-law index of the pre-shock density profile γ, and the multipoles a_ℓ of the angle-dependent shock position,

$$A_{20,\mathrm{shock}}^{\mathrm{E2}} \approx \frac{256\pi^{3/2}G}{5\sqrt{15}c^4} \rho_{\mathrm{p}} \left(\beta - 1\right) a_0^3 \left[(4 + \gamma)a_2\dot{a}_0 + \dot{a}_2 a_0\right],$$

$$(9)$$
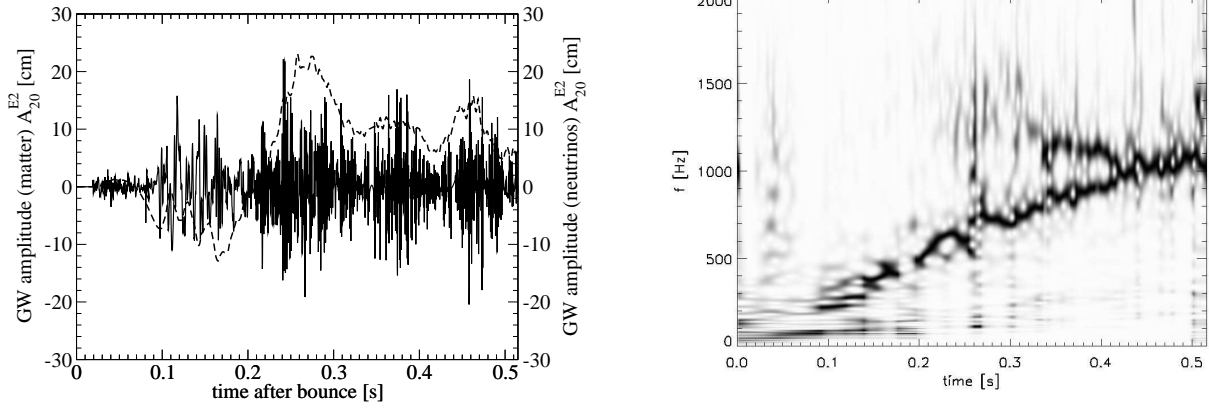
Figure 4. Left panel: Matter (solid lines) and neutrino (dashed lines) gravitational wave signals for model M15. Right panel: Normalized wavelet spectrum $\bar{\chi}(t, f)$ of the matter signal for model M15.
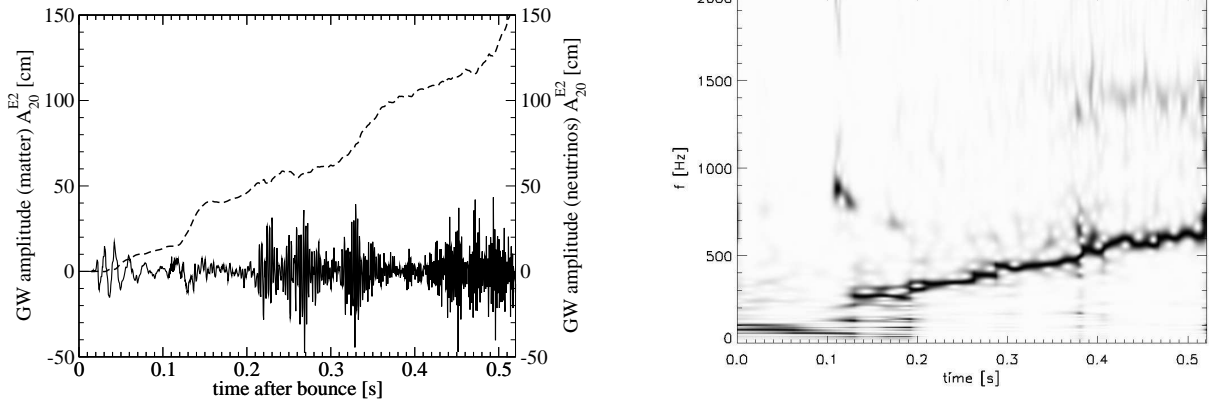
Figure 5. Left panel: Matter (solid lines) and neutrino (dashed lines) gravitational wave signals for model N15. Right panel: Normalized wavelet spectrum $\bar{\chi}(t, f)$ of the matter signal for model N15.

as derived in Appendix B. The multipole coefficients a_ℓ are defined in terms of the angle-dependent shock position and the ℓ-th Legendre polynomial as

$$a_\ell = \frac{2\ell + 1}{2} \int_0^\pi r_{\rm sh}(\theta) P_\ell(\theta) \, {\rm d} \cos\theta. \qquad (10)$$

With typical values for the early post-bounce phase ($\rho_{\rm p} \approx 10^9$ g cm^{-3}, $\gamma \approx -1.5$), the resulting values are more than an order of magnitude smaller than the observed amplitudes on the order of several 10 cm.

However, convection can be excluded as the direct source of the quasi-periodic signal as well, since the destabilizing entropy and lepton number gradients are erased very quickly, while the initial phase of gravitational wave emission lasts for several tens of milliseconds. The actual source of the signal can be determined by considering the integrand
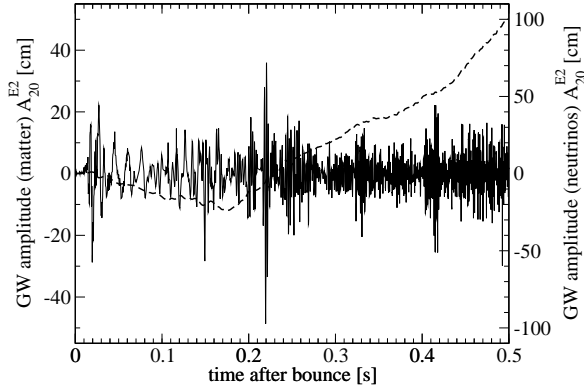
$$\psi = r^3 \sin\theta \frac{\partial}{\partial t} \left[S_r (3 \cos^2\theta - 1) + 3 r^{-1} S_\theta \sin\theta \cos\theta \right] \phi^6 \qquad (11)$$

in the quadrupole formula (1) for the matter signal in order to identify the main contributions to $A_{20}^{\rm E2}$ (cp. Murphy et al. 2009). By visualizing ψ (left half of Figure 7), waves or hydrodynamic mass motions responsible for gravitational wave emission can be identified fairly well. The largest contribution to $A_{20}^{\rm E2}$ comes from coher-

ent stripe-like patterns between 25 km and the shock. The underlying flow pattern appears to be dominated by propagating wavefronts (and not convective plumes), which emerge even more clearly when the partial time derivative $a = \partial v_r / \partial t$ of the velocity field is plotted (right panel of Figure 7). These can be identified as acoustic waves by their propagation speed and by the fact that the temporal variations δP and $\delta \rho$ of the pressure and the density obey the relation $\delta P/P \approx \Gamma \delta \rho/\rho$ (where Γ is the adiabatic exponent). The frequency of these waves is of the order of 100 Hz, which also accords well with the gravitational wave spectrum during this signal phase. In our model, prompt convection is thus only indirectly responsible for the quasi-periodic signal, either by directly initiating acoustic waves, or by instigating SASI activity, which also involves the propagation of acoustic waves in the post-shock region with the SASI frequency.

Both outgoing and ingoing waves (arising from partial reflection at the shock) appear to be present so that it is tempting to interpret these waves as transient p-modes in the post-shock region. It cannot be excluded, however, that the oscillatory motions in the post-shock regions also involve other (e.g. vorticity) waves. Along with the transitory nature of these motions, this precludes an unambiguous identification of the typical GW frequency with a definite mode frequency based on the present simulation data.

Figure 6. Left panel: Matter (solid lines) and neutrino (dashed lines) gravitational wave signals for model S15. Note that the scale for the matter signal (left vertical axis) is different from the scale for the neutrino signal (right vertical axis). Right panel: Normalized wavelet spectrum $\bar{\chi}(t, f)$ of the matter signal for model S15.
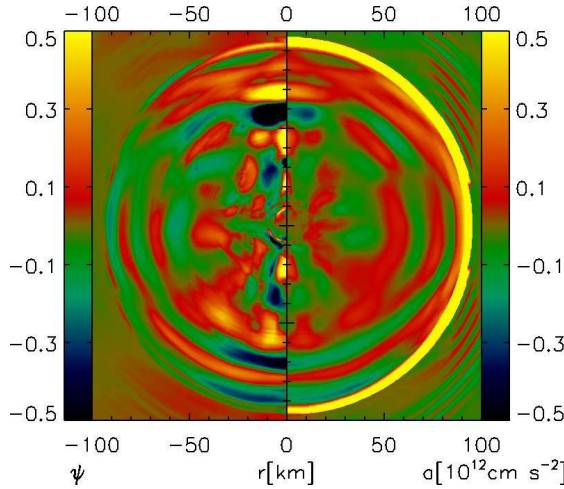
Figure 7. The dimensionless integrand ψ in the quadrupole formula (1) for the matter signal (left half of figure) and the time derivative $a = \partial v_r / \partial t$ (right half) of the radial velocity field 22 ms after bounce for model G15.
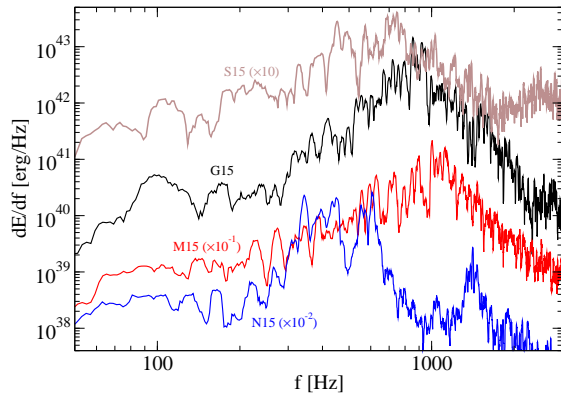
Figure 8. Gravitational wave energy spectra (matter signal only) for models G15 (black), M15 (red) N15 (blue), and S15 (brown) for the time interval from 20 ms to 520 ms after bounce. The Fourier transform has been carried out without a window function in order to retain the high-frequency contribution from the phase of strong gravitational wave emission after 400 ms in model G15. In order to better differentiate the curves, the spectra have been rescaled by a factor of 10^{-1}, 10^{-2}, and 10 for model M15, N15, and S15, respectively.
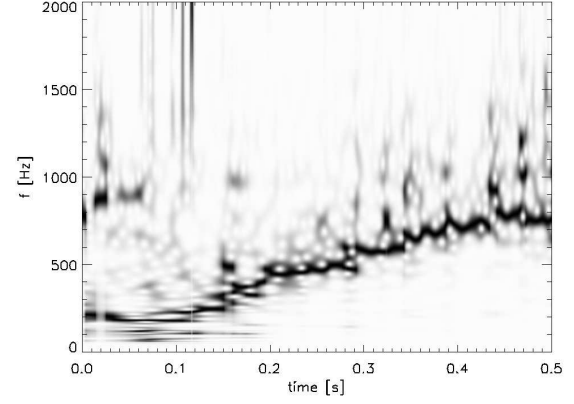
Figure 9. Maximum Brunt-Väisälä frequency f_p in the convectively stable region between the proto-neutron star convection zone and the gain layer as a function of time for models G15 (solid line), M15 (dashed) and N15 (dotted). f_p is a rather flat function of radius in this region, and the maximum value may therefore be taken as an estimate for the "typical" value of the Brunt-Väisälä frequency. The plot also shows the peak frequencies extracted from the wavelet spectra (Figures 3, 4, 5) at intervals of ≈ 50 ms (squares: model G15, circles: M15, triangles: N15).

4.2.2. *Effect of the GR Treatment on the Signal*

The amplitude and frequency of the quasi-periodic signal varies appreciably between the models investigated here. For the $15 M_\odot$ models with a different treatment of gravity (G15, M15, N15), the maximum amplitude ranges from 26 cm (G15) to < 2cm in model M15, where hardly any gravitational wave activity takes place during this phase. We believe, however, that these differences in amplitude may simply stem from a stronger or weaker excitation of $l = 2$ shock oscillations and acoustic waves in the different models. The differences are therefore not indicative of a systematic effect of the GR treatment on the strength of this signal. This conclusion is also supported by the fact that the early signal is much stronger in model M15LS-2D of Marek et al. (2009) (which only differs from model M15 by a higher angular resolution) than in model M15. Overall, the amplitudes in the GR case appear to be of similar magnitude as in Newtonian (Kotake et al. 2007; Murphy et al. 2009) and pseudo-Newtonian simulations (Marek et al. 2009; Yakunin et al. 2010) with peak amplitudes A_{20}^{E2} of

~ 40 cm (G11.2) and ~ 30 cm (G15).

On the other hand, the typical signal frequency is less affected by such stochastic variations, and is therefore a better indicator for systematic differences, which are indeed observed: The gravitational wave spectrum of the early signal peaks at a somewhat higher frequency of ≈ 100 Hz in the GR case (G11.2 and G15) compared to ≈ 60 Hz in the Newtonian case (N15). For model M15, the early signal is rather weak, but there is still a peak in the region around ≈ 70 Hz in the wavelet spectrum, which is in agreement with the result obtained by Marek et al. (2009) for their $15 M_\odot$ model with the EoS of Lattimer & Swesty (1991). There thus appears to be a tendency towards higher frequencies in the GR case. This frequency shift could be the result of a different width and location of the region affected by prompt post-shock convection (cp. Marek et al. 2009 for this line of reasoning in the context of EoS effects on the gravitational wave signal): While prompt convection develops in the region between enclosed masses of $0.61 M_\odot$ and $0.77 M_\odot$ in model G15, the corresponding range in model N15 is $0.66 M_\odot \ldots 0.83 M_\odot$ and $0.61 M_\odot \ldots 0.71 M_\odot$ in model M15 and in the Lattimer & Swesty run of Marek et al. (2009). Interestingly, Marek et al. (2009) found a similar shift towards higher frequencies with the stiffer nuclear equation of state of Hillebrandt & Wolff (1985), for which the spectrum of the early gravitational wave signal is remarkably similar to that of model G15.

The early GW signal from model S15 with simplified neutrino rates also shows a different frequency structure than that of G15. The dominant frequency is initially rather high (~ 200 Hz), but after 50 ms post-bounce, lower frequencies also appear in the spectrum. Again, the width of the layer affected by prompt convection is probably a factor responsible for this difference: In S15, there are two unstable regions, namely $0.77 M_\odot \ldots 0.88 M_\odot$ and $0.96 M_\odot \ldots 1.07 M_\odot$, i.e. the convective region contains a significantly larger mass and is located further outside than in G15. It is noteworthy that the simplified neutrino rates change the entropy and lepton number profiles in the early post-bounce phase so drastically that the dynamics of prompt convection and the GW signal are altered significantly.

Especially during the later phases of the prompt signal ($20 \ldots 100$ ms after bounce) when the (gravito-)acoustic waves propagate throughout the entire region between the PNS and the shock, the GW frequency may also be influenced by the sound crossing time-scale or (if a vortical-acoustic loop is involved in the shock oscillations) the advection time-scale for that region. This could account for the frequency shift in the Newtonian case. Here, the shock radius, and hence the sound crossing time-scale as well as the advection time-scale are significantly larger than in the GR case during the relevant phase, which suggests lower GW frequencies.

We refrain from a more quantitative analysis of the early GW signal frequencies here. While it is obvious that the width and location of the region of prompt convection as well as the shock position and PNS radius affect the parameters relevant for oscillations involving trapped (gravito-)acoustic waves (and perhaps vorticity waves) inside an accretion shock, i.e. the local sound speed, the gravitational acceleration, and the radial velocity, there is no simple quantitative theory for the early

GW frequencies (different from the GW signal from hot-bubble convection discussed in the next section).

4.3. GW Signal from Hot-Bubble Convection and the SASI

4.3.1. Model Comparison – Shift of Characteristic Frequencies

After the early quasi-periodic signal has subsided, a phase of relatively weak GW emission ensues, and even when hot-bubble convection starts, the GW wave activity may not increase immediately. The onset of stronger GW emission from hot-bubble convection appears to be strongly model-dependent with no clear connection to the dynamics. In model G11.2, the explosion is already underway when the GW amplitude starts to increase significantly 200 ms after bounce, and in the Newtonian model N15, there is a similarly long delay. At the other end of the scale, we find model S15, where there is no gap between the early quasi-periodic signal and the signal from hot-bubble convection (which is helped by the fact that the gain region already develops at ~ 60 ms in this model).

Due to the stochastic nature of the signal, the amplitudes of the different models should be compared with some caution. All models exhibit amplitudes on the order of several 10 cm, which is roughly consistent with earlier pseudo-Newtonian studies with sophisticated neutrino transport (Müller et al. 2004; Marek et al. 2009; Yakunin et al. 2010). Nevertheless, two general trends emerge: As exemplified by models G11.2 and G15, the phase of strongest gravitational wave emission begins when the shock starts to expand again and lasts. This phase lasts for about 200 ms, after which point the stochastic signal largely subsides. Furthermore, the gravitational wave amplitude is loosely correlated with the mass in the gain region and the convective energy, which is why the pessimistic, non-exploding model M15 is characterized by somewhat smaller amplitudes than G15, a model with stronger convection and a larger gain region (cp. Müller et al. 2012b). For the same reason, model S15 with simplified neutrino rates and less favorable heating conditions also shows smaller amplitudes than model G15 in general.

As for the early quasi-periodic signal, the gravitational wave spectra reveal the effect of general relativity much more clearly than the amplitudes. A sizable frequency shift in GR compared to the Newtonian and the effective potential approximation can be seen both in the wavelet spectra in Figures 3–5 as well as in the time-integrated spectral energy distribution $\mathrm{d}E/\mathrm{d}f$ (see Equation 7) for the first 500 ms after bounce shown in Figure 8. In the GR run, the peak is clearly located at a higher frequency than in the purely Newtonian case, but the peak frequency remains somewhat smaller than with the effective potential approach. To quantify these differences, we compute the median f_M of the spectral energy distribution $\mathrm{d}E/\mathrm{d}f$, which is implicitly defined by the condition

$$\int_0^{f_M} \frac{\mathrm{d}E}{\mathrm{d}f} \mathrm{d}f = \frac{1}{2} \int_0^\infty \frac{\mathrm{d}E}{\mathrm{d}f} \mathrm{d}f, \qquad (12)$$

i.e. f_M is the frequency below which half of the total en-

ergy in gravitational wave is radiated. We obtain values of $f_M = 920$ Hz for model G15, 1100 Hz (+20%) for model M15, and 510 Hz (−44%) for the purely Newtonian model N15. The same ordering is observed in the wavelet spectra (Figure 3–5) throughout the simulation once hot-bubble convection starts. As for the early quasi-periodic signal, general relativistic effects therefore considerably affect the gravitational wave spectrum, leading to significantly higher frequencies (by ∼ 80%) than in the purely Newtonian case, while the effective potential approach proves to be accurate to within ∼ 20%. Again the effects of general relativity prove to be of similar magnitude as EoS effects (for which we refer to Marek et al. 2009) and emerge as a major factor in determining the gravitational wave spectrum.

Unlike for the early quasi-periodic signal, the effect of the simplified neutrino rates is not very pronounced. For model S15, we obtain a value of $f_M = 840$ Hz, which is somewhat lower than for model G15. At a given time, the dominant frequencies are relatively similar for both models (Figures 3, 6), so the crucial factor for the shift of the median frequency must be the onset of the explosion in model G15: This leads to enhanced GW emission after 400 ms and hence a higher weighting factor for late-time high-frequency emission than for model S15.

We note that models G11.2 and G15 show very similar trends in their wavelet spectra, but refer the reader to Section 5 for a more thorough discussion of the progenitor dependence.

4.3.2. *Origin of Frequency Shift in GR*

The dependence of the typical frequency of the gravitational wave signal from hot-bubble convection and SASI activity can be understood by considering the dominant emission mechanism during this phase. Marek et al. (2009) and Murphy et al. (2009) found that anisotropic mass motions in the convectively stable region above the proto-neutron star surface actually account for the bulk of the signal (although these motions are in turn instigated by convection and the SASI). While Murphy et al. (2009) suggested the deceleration of infalling convective plums as a direct source for the gravitational wave signal, Marek et al. (2009) also mention surface g-mode oscillations excited by the downflows as a source. Both mechanisms can work in tandem, and one may speculate that the continuous narrow emission bands in Figures 2–6 are associated with a time-variable, but relatively stable g-mode frequency, whereas the deceleration of plumes with random frequency and penetration depth is responsible for the more noisy part of the spectrum above this band.

In either case, an anisotropic, buoyancy-driven flow is responsible for the emission of gravitational waves, and the typical angular frequency of the signal is therefore approximately given by the buoyancy or Brunt-Väisälä-frequency N in the convectively stable region between the neutrinosphere and the gain radius (as Murphy et al. 2009 explicitly verified for their model). As we shall demonstrate, the GR treatment systematically affects the buoyancy frequency in a way that accounts for the observed frequency differences.

In the Newtonian case, the buoyancy frequency is given

by the familiar expression (see, e.g., Aerts et al. 2010),

$$N^2 = \frac{1}{\rho}\frac{\partial \Phi}{\partial r}\left(\frac{1}{c_s^2}\frac{\partial P}{\partial r} - \frac{\partial \rho}{\partial r}\right), \qquad (13)$$

where Φ is the gravitational potential, ρ the (rest-mass) density, c_s the sound speed, and P the pressure. Equation (13) is not applicable in the general relativistic case, however, because the underlying equations of hydrodynamics are different. The relativistic expression for the Brunt-Väisälä-frequency, derived in Appendix C for the gauge used in VERTEX-COCONUT, reads

$$N^2 = \frac{\partial \alpha c^2}{\partial r}\frac{\alpha}{\rho h \phi^4}\left(\frac{1}{c_s^2}\frac{\partial P}{\partial r} - \frac{\partial \rho(1 + \epsilon/c^2)}{\partial r}\right), \qquad (14)$$

which contains correction terms involving the lapse function α, the conformal factor ϕ, the specific internal energy ϵ and the specific relativistic enthalpy $h = 1 + \epsilon/c^2 + P/(\rho c^2)$. Note that we formulated Equation (14) in terms of α, ϕ, and h in their non-dimensional form.

In Figure 9, we compare the real frequency $f_p = N/2\pi$ (the "plume frequency" of Murphy et al. 2009) corresponding to the buoyancy frequency in the convectively stable neutron star surface region for models G15, M15, and N15 and also show the peak frequency extracted from the wavelet spectrum $\bar{\chi}$ at selected points in time. We clearly observe the same ordering of the models for f_p as for the peak frequency, although f_p generally overestimates the actual frequency of the spectrum by up to 30% (as already noticed by Murphy et al. 2009).[2]

The different buoyancy frequencies in G15, M15, and N15 thus account nicely for the effect of the GR treatment on the GW spectrum, and the terms responsible for the shift of f_p can be readily identified: In the Newtonian approximation (model N15), the neutron star is less compact than in GR due to the lack of non-linear strong-field effects, and the gravitational acceleration term in $\partial \Phi/\partial r$ Equation (13) is therefore smaller than the corresponding term $\partial \alpha c^2/\partial r$ in GR (or $\partial \Phi/\partial r$ in the effective potential approximation). f_p, and hence the GW peak frequency is *underestimated*. The different compactness of the proto-neutron star is most likely also responsible for the discrepancy between our Newtonian results and those of Murphy et al. (2009), who obtained even lower GW frequencies (e.g. only 200 . . . 300 Hz at 500 ms): Their use of a stiff EoS (Shen et al. 1998) and of a parametrized neutrino cooling and heating scheme, which does not allow for the loss of energy and lepton number from the PNS core, both tend to underestimate the contraction of the proto-neutron star.

On the other hand, the effective potential approach (model M15) gives a very good approximation for the compactness of the proto-neutron star ($\partial \Phi/\partial r \approx \partial \alpha c^2/\partial r$), but still fails to reproduce the correct peak frequency because the effects of relativistic kinematics are not taken into account. In GR, the correction factor $\alpha h^{-1}\phi^{-4}$ in Equation (14) reduces f_p by about 15% to 20%, which largely explains the lower frequencies in

---

[2] The fact that the GW peak frequency is consistently lower than f_p is consistent with the hypothesis that the dominant frequency seen in the GW spectrum is actually that of a surface g-mode oscillation, since the buoyancy frequency provides an upper bound for the g-mode frequency (see, e.g.,Kippenhahn & Weigert 1990; Aerts et al. 2010).

model G15 compared to M15. In addition, the slightly higher neutrino luminosities and mean energies in model G15 also correlate with a somewhat more shallow density gradient in the neutron star surface region and thus reduce f_p and the typical gravitational wave frequency even a little further.

These arguments indicate that gravitational wave spectra from the later ($\gtrsim 150$ ms) post-bounce phase with an accuracy better than $\sim 20\%$ in frequency space can only be obtained within the framework of general relativistic hydrodynamics, since both the Newtonian and the pseudo-Newtonian approximation suffer from an *intrinsic* accuracy limit.

4.3.3. *Relation between PNS Properties and the Characteristic GW Frequency*

Could the characteristic GW frequency, which emerges clearly from the wavelet spectra in Figures 3–5 provide clues about properties of the proto-neutron star, such as its mass, compactness, or surface temperature? A simple analytic estimate for f_p based on Equation (14) can shed light on this question.

The metric functions α and ϕ in Equation (14) can be approximated in terms of the proto-neutron star mass M and radius R as $\alpha \approx \ln\alpha \approx \phi^{-2} \approx 1 - GM/(Rc^2)$ at the proto-neutron star surface, and the pressure and density gradients can be found by assuming a roughly isothermal stratification (with temperature T) in the convectively stable neutron star surface layer. Furthermore, an ideal gas equation of state can be used as non-relativistic[3] baryons dominate the pressure in the relevant region. The gradient terms in Equation (14) can then be immediately obtained in terms of T and the neutron mass m_n from the equation of hydrostatic equilibrium,

$$\frac{\partial P}{\partial r} \approx \frac{\partial}{\partial r}\left(\frac{\rho kT}{m_n}\right) = -\rho\frac{\partial \ln\alpha}{\partial r}. \qquad (15)$$

Employing the relation $c_s^2 = \Gamma kT/m_n$ for the speed of sound (Γ being the adiabatic index), we then arrive at the following expression for f_p,

$$f_p = \frac{N}{2\pi} = \frac{1}{2\pi}\frac{GM}{R^2}\sqrt{\frac{(\Gamma-1)m_n}{\Gamma k_b T}}\left(1 - \frac{GM}{Rc^2}\right)^{3/2}, \quad (16)$$

where Γ is the adiabatic index in the proto-neutron star surface region, and m_n is the neutron mass. The mean energy $\langle E_{\bar{\nu}_e}\rangle$ of electron antineutrinos may be used as a proxy for the temperature (with additional redshift corrections, i.e. $\langle E_{\bar{\nu}_e}\rangle \approx 3.151\alpha(R)T$), and one thus obtains a fairly accurate formula for the evolution of the dominant GW frequency $f_{\rm peak}$:

$$f_{\rm peak} \approx \frac{1}{2\pi}\frac{GM}{R^2}\sqrt{1.1\frac{m_n}{\langle E_{\bar{\nu}_e}\rangle}}\left(1 - \frac{GM}{Rc^2}\right)^2. \qquad (17)$$

For our two exemplary models G11.2 and G15, Figure 10 shows that Equation (17) is in fairly good agreement with the measured frequencies. The critical parameters regulating $f_{\rm peak}$ are thus i) the surface gravity, ii) the surface temperature, and iii) the compactness parameter

---

[3] This implies $\epsilon \ll 1$.

GM/Rc^2 of the proto-neutron star. Since $f_{\rm peak}$ also depends on the thermal properties of the PNS surface layer, gravitational waves from the accretion phase probably cannot provide an unambiguous probe for the bulk properties of the proto-neutron star (mass, radius). On the other hand, the theory underlying Equation (17) suggests that 2D models already capture the frequency structure of the GW signal well: With the buoyancy frequency in the convectively stable region determining the GW spectrum (probably via the frequency of the $\ell = 2$ surface g-mode) we expect the same dominant frequency in 3D in the absence of rotation (because of the degeneracy of oscillation modes with different m).

Equation (17) illustrates that $f_{\rm peak}$ is sensitive to factors that affect the contraction and thermal evolution of the proto-neutron star, such as the EoS and the neutrino treatment. The different neutrino rates in model S15 are not critical in this respect since they affect the proto-neutron star surface temperature only on a very moderate level (see paper II). More radical approximations in the neutrino treatment could potentially have a sizable impact, however, provided that they change the proto-neutron star surface temperature and the neutrino mean energies considerably. The neutrino treatment (multi-group variable Eddington factor transport vs. parametrized heating and cooling) along with the different equation of state may also partially account for the differences of our Newtonian model N15 to the models of Murphy et al. (2009). For the dependence of $f_{\rm peak}$ on the progenitor, we refer the reader to Section 5.

4.4. *Explosion Phase – Proto-Neutron Star Convection and Late-Time Bursts*

As established by Murphy et al. (2009) and Yakunin et al. (2010), the emission of high-frequency gravitational waves subsides to a reduced level once the shock accelerates outwards because the excitation of oscillations in the proto-neutron star surface by violent convective motions in the hot-bubble region largely ceases. This is well reflected in the GW signals of models G11.2 and G15 (Figures 2, 3) in the *initial* phase of the explosion, as the GW amplitude drops noticeably after 400 ms and 600 ms, respectively. However, the surface g-mode oscillations remain the dominant source of high-frequency gravitational waves during this phase: The wavelet spectra clearly show that the late-time signal comes from the same emission band as the signal from the accretion phase (which shifts continuously to higher frequencies as the neutron star contracts). An analysis of the integrand ψ in the quadrupole formula (1) as in Section 4.2.1 also confirms that aspherical motions in the proto-neutron star surface region are still the dominant source of gravitational waves. Proto-neutron star convection now provides an excitation mechanism for the oscillations (Müller & Janka 1997; Marek et al. 2009; Murphy et al. 2009; Müller et al. 2012c), but due the subsonic character (with Mach numbers $\lesssim 0.05$) of the convective motions, the GW amplitude $A_{20}^{\rm E2}$ remains rather small.

However, model G11.2 contradicts the established picture of subsiding GW emission during the explosion. For this progenitor, we observe several "bursts" of stronger gravitational wave emission later in the explosion phase on at least three occasions (630 ms, 790 ms, and 820 ms),
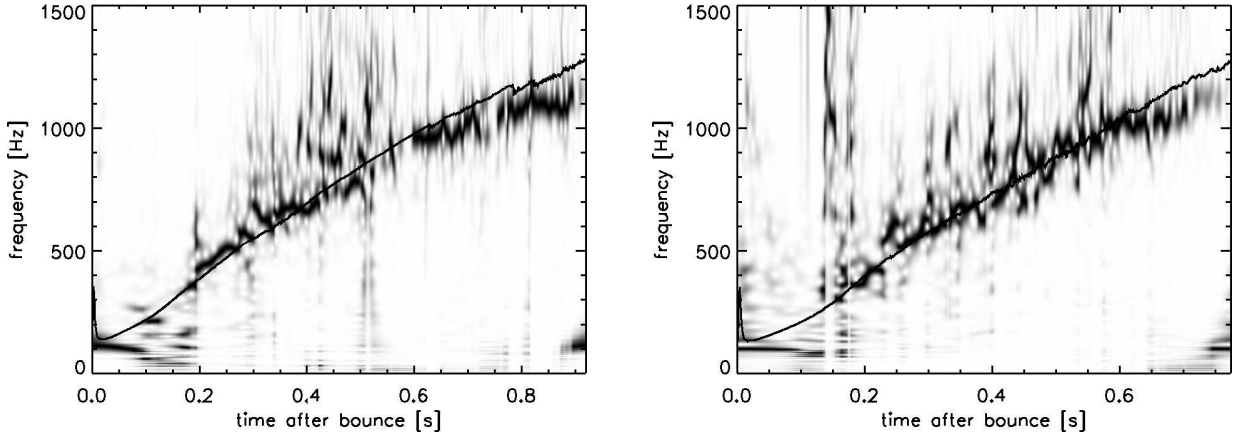
Figure 10. Comparison of the wavelet spectra (identical to those in Figures 2 and 3, respectively) of model G11.2 (left)and G15 (right) and the prediction of Equation (17) for the typical gravitational wave frequency in terms of the proto-neutron star mass and radius and the mean energy of electron antineutrinos measured by an observer at infinity. Equation (17) describes the evolution of the typical frequency fairly well and only overestimates $f_{\rm peak}$ somewhat at late times.
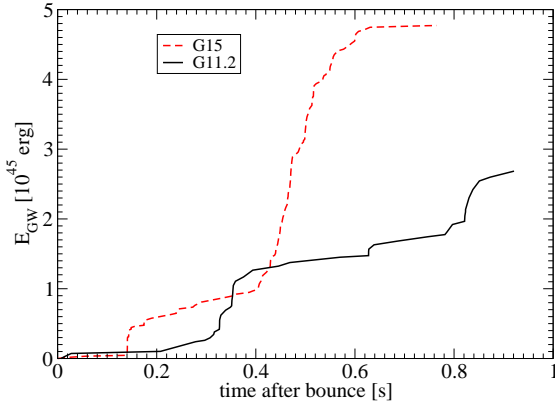
Figure 11. Energy $E_{\rm GW}$ radiated in gravitational waves as function of time for the explosion models G11.2 (black solid line) and G15 (red dashed line) for the entire duration of the simulation. For model G15, most of the energy is radiated around the onset of the explosion between 400 ms and 600 ms after bounce. By contrast, late-time GW bursts carry a sizable fraction of the radiated energy in the case of model G11.2.

during which the amplitude can become comparable to that coming from the phase of hot-bubble convection. About 40% of the GW energy is emitted later than 600 ms after bounce (Figure 11), which is in stark contrast to the more vigorous explosion in model G15 with faster shock expansion. These bursts occur when matter falls back onto the proto-neutron star through a newly developing downflow, which excites g-mode oscillations in the proto-neutron star surface region (Figure 12). The formation of new downflows in the explosion phase is a consequence of the small explosion energy of model G11.2 (see paper II), and one could speculate that low-energy fallback supernovae may generally reveal themselves through such multiple GW burst episodes. While the development of such an accretion downflow may be facilitated by the constraint of axisymmetry, it is conceivable that funnel- or plume-shaped downdrafts may impinge on the proto-neutron star in a similar manner in a weak explosion in 3D (cf. some 3D results of Müller et al. (2012c), where long-lasting accretion after the explosion was associated with time-dependent accretion downdrafts.). Given the fact that Takiwaki et al. (2012) do not obtain faster shock propagation in 3D than

in 2D for this particular progenitor in their simulations using the IDSA scheme, it is not unlikely that the explosion energies will remain low as in our 2D model (a few 10^{49} erg, see Müller et al. 2012b) and that late-time bursts seen in our simulations will survive in 3D. Without detailed 3D simulations of this sort, however, it is unclear how massive the downdrafts can become and what GW burst amplitudes they can cause.

Several interesting features of these late-time bursts should be noted: Between the few instances where new accretion downflow develop, aspherical mass motions above the proto-neutron star surface are apparently not strong enough to produce significant noise in the GW signal, and the g-mode frequency therefore emerges much more cleanly from the spectrum during the late time GW bursts than in the accretion phase. The narrow-band character of the spectrum (see Figure 2 and the red curve in Figure 14) is potentially helpful both for the detection of the GW signal as well as for the interpretation of the data (e.g. by allowing for a clearer discrimination of different equations of state on the basis of the g-mode frequency). Moreover, the bursts directly coincide with an enhancement of the electron neutrino and antineutrino luminosities and mean energies as shown in Figure 13: When the newly-formed downflows bring fresh material into the cooling region, the luminosity of ν_e and $\bar{\nu}_e$ increases abruptly by up to $\sim 20\%$, and the mean energy of the emitted neutrinos jumps by up to ~ 1 MeV. Such correlations between the neutrino and GW signals probably merit further investigation, but a deeper analysis taking into account both the observer position and the detailed anisotropies in the neutrino radiation field in the manner of Müller et al. (2012c) will not be attempted here. The anisotropic neutrino emission will be discussed more thoroughly in a subsequent publication.

4.5. The Tails in the Matter and Neutrino Signals

At late times, the gravitational wave signals of our models G11.2 and G15 exhibit the same low-frequency features that have been observed in previous studies: The matter signal develops an offset or "tail" which has been ascribed to aspherical shock propagation (Murphy et al. 2009; Yakunin et al. 2010), with prolate/oblate explosions leading to positive/negative amplitudes. This off-
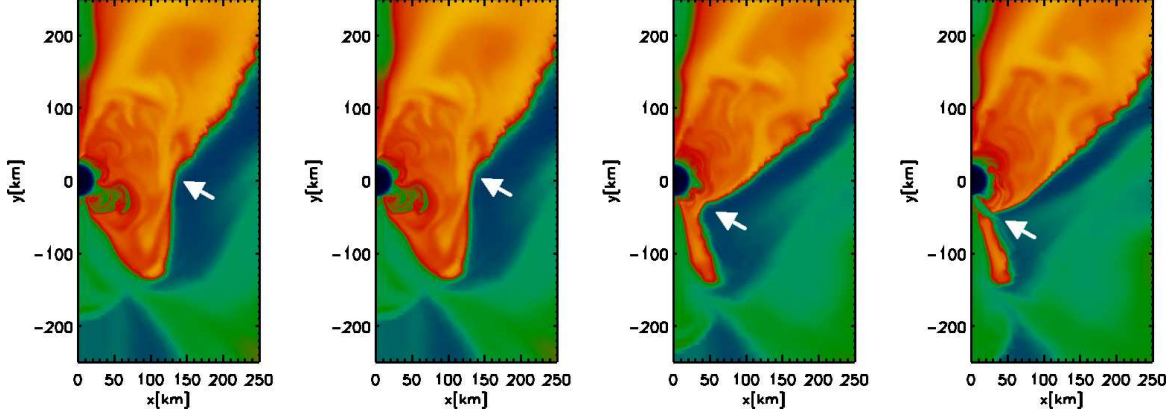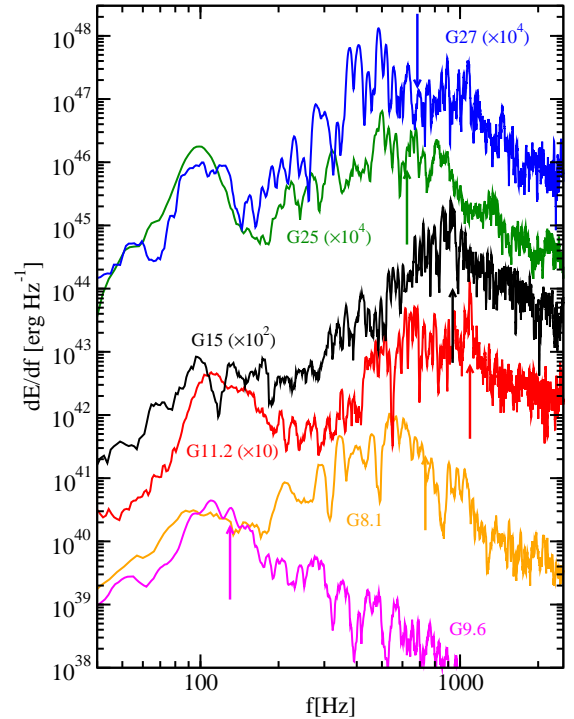
Figure 12. Snapshots of the entropy s in the region around the proto-neutron star at post-bounce times of 812.3 ms, 816.5 ms, 819.7 ms, and 821 ms, depicting the formation of a new downflow by material falling through a hot bubble of neutrino-heated material. To guide the eye, the dent in the high-entropy bubble, which eventually develops into the new downflow is highlighted by a white arrow in each panel. The values of the entropy range from $0k_b$/nucleon (black) to $35k_b$/nucleon (yellow). Due to its high infall velocity, the downflow overshoots far into the convectively stable proto-neutron star surface layer, exciting violent oscillations. The GW burst occurring at this time can be seen in Figures 2 and 13.
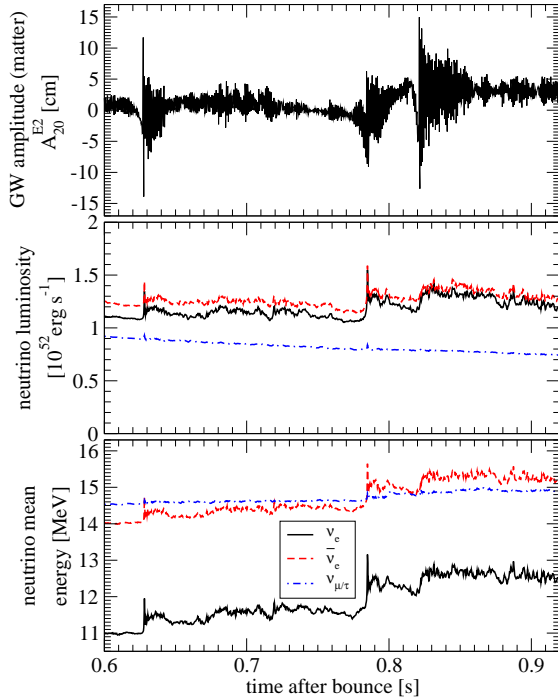
Figure 13. Correlation of late-time bursts in the GW signal and the neutrino signal: The top panel shows the GW amplitude A_{20}^{E2} as a function of time for model G11.2 between 600 ms and 920 ms after bounce. The middle panel displays the neutrino luminosity of ν_e (black solid line), $\bar{\nu}_e$ (red, dashed), and $\nu_{\mu/\tau}$ (blue, dash-dotted) – defined as the neutrino energy flux integrated over all emission directions as measured at an observer radius of 400 km. The bottom panel shows the direction-averaged mean energy of neutrinos at the same observer radius.

Figure 14. Gravitational wave energy spectra (matter signal only) for the relativistic models G8.1 (orange), G9.6 (magenta), G11.2 (red), G15 (black), G25 (green), and G27 (blue), for the entire duration of the simulation. Note that some of the spectra have been rescaled by a factor given along with the model designation. The Fourier transform has been carried out without a window function in order to retain the high-frequency contributions towards the end of some simulations. The spectra reflect larger amplitudes of the early quasi-periodic signal (around ~ 100 Hz) in models G11.2, G25, and G27. For model G9.6, there is almost no high-frequency signal from hot-bubble convection. For G11.2, the sharp peak slightly above 1 kHz emerges in the spectrum due to late-time GW bursts.

set is of the order of $10 - 15$ cm for model G15 (which is consistent with its prolate explosion geometry), while only a small offset of ≈ 3 cm develops for model G11.2 at rather late times due to the small shock deformation. These amplitudes are consistent with a direct numerical evaluation of Equation (B3)[4], which confirms that as-

---

[4] Note that Equations (9,B6) cannot be used to evaluate the gravitational wave amplitude due to aspherical shock propagation for model G15 because the Legendre coefficient a_1 of the angle-dependent shock position $r(\theta)$ is of the same order as a_0, and the assumptions used to derive Equations (9,B6) therefore break down.

pherical shock propagation is indeed responsible for the offset in the signal.

However, as in Yakunin et al. (2010) the "tail" signal is much weaker than the similar tail-like signal from the anisotropic emission of neutrinos. Models G11.2 and G15 both develop long-lived polar downflows that subsist well into the explosion phase and lead to a sustained quadrupolar emission anisotropy over several hundreds of milliseconds; in model G15 the running average of the anisotropy parameter α_ν (Equation 5) over 50 ms can become as large as 0.02. This is in striking contrast to model M15 with many alternating episodes of enhanced emission from the polar and the equatorial region. It is very likely, however, that stochastic model variations affect the neutrino-generated gravitational wave signal considerably; model M15, e.g., is distinguished from the L&S model of Marek et al. (2009) only by a different angular resolution, yet Marek et al. (2009) obtained a large negative signal amplitude due to the predominant emission of neutrinos from the equatorial region. However, even in model M15, the typical amplitude of the neutrino-generated signal is larger than the typical signal from aspherical shock propagation, which will probably always remain a subdominant contribution to the low-frequency part of the spectrum.

5. PROGENITOR DEPENDENCE OF THE GW SIGNAL

After having discussed the different phases of GW emission for models G11.2 and G15, we now turn to the progenitor dependence of the GW signal. Models G8.1–G27 exhibit a widely different behavior in the accretion and (where applicable) the explosion phase, and thus illustrate how the GW emission is correlated with important parameters characterizing the dynamical evolution such as the explosion time, the proto-neutron star mass, or the mass accretion rate. While the precise dynamics of individual progenitors (time and energy of the explosion, etc.) may depend on uncertainties in the modeling (3D effects, progenitor structure, etc.), the spectrum of models presented here already reveals such general trends very well. An overview over the waveforms for models G8.1–G27 is given in Figure 15, and time-integrated GW energy spectra are shown in Figure 14. Table 2 summarizes important characteristic numbers for the waveforms and spectra.

5.1. *Progenitor Dependence of Waveforms*

Figure 15 and Table 2 illustrate a few general trends in the GW signals: GW activity tends to increase for models with higher accretion rate $\dot{M}$ during the phase of convective and SASI activity. Table 2 shows that except for model G25 there is a strong correlation between the accretion rate $\dot{M}_{90}$ at a post-bounce time of 90 ms (typically close to the onset of strong convection/SASI) and the total gravitational wave energy E_{GW} as well as the maximum amplitude $A_{20,\mathrm{max}}^{\mathrm{E2}}$. This correlation is reasonable, since the typical GW amplitude depends on the mass in the gain and cooling regions participating in violent aspherical motions and g-mode activity, respectively, Both of these masses in turn regulated by the accretion rate. Naturally, $\dot{M}_{90}$ should not be understood as a single unambiguous parameter regulating the GW emission; it is rather the overall evolution of $\dot{M}$ that is relevant.

Because of vastly different accretion rates, models G9.6 and G27 constitute two extreme cases on the scale of GW emission: In model G9.6, the accretion rate drops so quickly that there is almost no signal from hot-bubble convection, and only the early quasi-periodic signal remains. Moreover, although there is some convective overturn in the ejecta in this model, the rather rapid explosion largely precludes the excitation of PNS surface g-modes by downflows or accretion downdrafts. The matter affected by overturn is blown out rather quickly ahead of the developing neutrino-driven wind (cp. top right panel of Figure 1).

By contrast, a lot of mass is involved in strong SASI oscillations prior to the onset of the explosion in model G27 (bottom right panel of Figure 1). Moreover, the shock does not expand as rapidly afterwards, thus allowing violent aspherical motions to continue for several hundreds of milliseconds beyond the onset of the explosion. Consequently, the energy emitted into gravitational waves is as high as 2×10^{46} erg for this model.

While the models G8.1, G11.2, and G15 fit nicely into a continuum between these extreme cases, model G25 shows *less* GW activity than model G27 although it is characterized by even higher mass accretion rates as well as by continuing SASI activity (bottom left panel of Figure 1). This reversal of the aforementioned trend is related to fact that G25 does not develop an explosion within the simulation time. GW emission is typically strongest around the onset of the explosion (G8.1, G11.2, G15, and G27), when the mass in the gain region increases considerably and aspherical motions in the postshock region become most violent (i.e. reach the highest velocities) before being quenched again during the later phases of shock expansion. This phase is lacking in model G25, and the strong retraction of the shock instead reduces the mass in the gain region so that the GW amplitude is strongly attenuated during the later evolution. Moreover, the relatively pure $\ell = 1$ SASI mode seen in model G25 may not be very efficient in exciting $\ell = 2$ perturbations in the flow to which the GW amplitude is sensitive.

The overall trends in the progenitor dependence suggested by the six models G8.1–G27 can thus be summarized as follows: GW emission tends to become stronger with increasing mass accretion rate. In addition, both a strong shock retraction and a very rapid explosion can quench GW activity.

5.2. *Progenitor Dependence of GW Spectra*

To characterize the spectral properties of models G8.1–G27, we show time-integrated energy spectra in Figure 14, for which we give the median frequency f_M in Table 2. Moreover, we list the dominant emission frequencies f_{250}, f_{300}, and f_{400} around 250 ms, 300 ms, and 400 ms after bounce to show the time-frequency evolution of the GW signals.

For the early quasi-periodic signal, which emerges as a low-frequency peak in the curves of Figure 14, we find no significant progenitor dependence. This signal component always peaks around 100 Hz in our models. The later signal from convection and the SASI shows somewhat larger variations. The typical emission frequencies f_{250}, f_{300}, and f_{400} vary by $\sim 30\%$, and tend to be highest for model G25. Considering that we cover a very wide

Table 2
Progenitor dependence of the GW signal

Model	M_{90}[a]	E_{GW}[b]	$A_{20,max}^{\mathrm{E2}}$[c]	f_{250}[d]	f_{300}[e]	f_{400}[f]	f_M[g]	M_{PNS}[h]	t_{expl}[i]
	$(M_\odot\,\mathrm{s}^{-1})$	$(10^{45}\ \mathrm{erg})$	(cm)	(cm)	(cm)	(Hz)	(Hz)	$(M_\odot)$	(ms)
G8.1	0.38	0.36	45	540	600	—	730	1.37	177
G9.6	0.09	0.0032	13	—	—	—	130	1.36	125
G11.2	0.57	2.7	52	570	580	680	1100	1.35	213
G15	1.08	4.8	70	520	580	710	950	1.58	569
G25	1.80	1.2	77	660	750	900	620	2.01	—
G27	1.44	20	253	580	700	860	680	1.77	209

[a]Mass accretion rate 90 ms after bounce.
[b]Energy of radiated gravitational waves.
[c]Maximum GW amplitude of the matter signal.
[d]Dominant emission frequency 250 ms after bounce.
[e]Dominant emission frequency 300 ms after bounce.
[f]Dominant emission frequency 400 ms after bounce.
[g]Median frequency of the GW energy spectrum.
[h]Baryonic mass of proto-neutron star by the end of the simulation.
[i]Explosion time, defined by the instance when the average shock radius $\langle r_{\mathrm{sh}} \rangle$ reaches 400 km.

range in PNS masses from $\sim 1.36 M_\odot$ (G9.6, G11.2) to $\sim 2.0 M_\odot$ (G25), this variation may seem astonishingly small. This can be understood as a partial cancellation of terms in Equation (17) for the dominant emission frequency:

$$f_{\mathrm{peak}} \approx \frac{1}{2\pi} \frac{GM}{R^2} \sqrt{1.1 \frac{m_n}{\langle E_{\bar{\nu}_e} \rangle}} \left(1 - \frac{GM}{Rc^2}\right)^2. \qquad (18)$$

While the surface gravity GM/R^2 is systematically larger for more massive and compact neutron stars, the proto-neutron star surface temperature is also higher, and the general relativistic correction term $(1 - GM/(Rc^2))^2$ is smaller. The remaining net change is typically moderate, as illustrated by G11.2 and G25 as rather extreme examples in Figure 16: Although the surface gravity is higher by up to $\sim 90\%$ in model G25, f_{peak} is only lower only by $\sim 35\%$ in model G11.2. Among the less massive proto-neutron stars (models G8.1, G11.2, G15), the differences are far less pronounced. The variation between progenitors is similar to that found by Murphy et al. (2009), although the absolute values for the frequencies are very different (since Murphy et al. 2009 lacked self-consistent neutrino transport and GR in their simulations, and used different progenitors as well as a different EoS).

When we consider time-integrated GW energy spectra (Figure 14), the relation between PNS and GW properties becomes more complicated, however. We observe the highest median frequency of $f_M = 1100$ Hz for model G11.2, while we find relatively low values between 600 Hz and 700 Hz for G25 and G27, although these two models have higher values for f_{250}, f_{300}, and f_{400}. This reversal occurs because much of the gravitational wave emission in G11.2 happens after the onset of the explosion in late-time bursts (see Section 4.4). GW waves with relatively high frequencies therefore contribute more strongly to the spectrum than in models such as G25 and G27. These late-time bursts are distinctly visible as a peak around 1100 Hz for G11.2 in Figure 8. For model G15, the situation is somewhat similar, because the bulk of GW emission occurs around 500 ms due to the rather late explosion. Model G9.6 constitutes another extreme because the high-frequency component of the spectrum

is largely absent, resulting in a low median frequency of $f_M = 130$ Hz.

Our results demonstrate that time-integrated spectra are the result of a somewhat complicated interplay between the time of strongest GW emission and the time-dependence of the dominant emission frequency. This implies that time-integrated spectra are even more difficult to relate to PNS properties than f_{peak} (cp. Section 4.3.3).

6. SUMMARY AND CONCLUSIONS

Based on several recent two-dimensional relativistic explosion models (Müller et al. 2012b) for non-rotating progenitors between $8.1 M_\odot$ and $27 M_\odot$, we studied the GW signal of core-collapse supernovae from the early post-bounce phase well into the explosion phase. We not only provided gravitational waveforms from GR hydrodynamics simulations with sophisticated multi-group neutrino transport for the first time, but also analyzed the impact of the GR treatment (GR vs. effective potential approach vs. Newtonian approximation) and of the neutrino physics input on the GW signal by means of three complementary (non-exploding) simulations of the $15 M_\odot$ progenitor.

In all phases, we found that GR has a sizable impact on the GW spectrum. For purely Newtonian models, we found that the typical GW frequency during the phase of hot-bubble convection is severely underestimated (by $40\% \ldots 50\%$) compared to the GR case, while it tends to be overestimated by $\sim 20\%$ in the effective potential approach. We determined that this is the results of *systematic* differences of the buoyancy frequency in the proto-neutron star surface region (which approximates the typical GW frequency as pointed out by Murphy et al. 2009). In the Newtonian approximation, the smaller compactness and surface gravity of the neutron star lead to a lower buoyancy frequency compared to GR, while the effective relativistic potential approach fails to correctly reproduce the frequency of oscillations in the proto-neutron star surface because of missing relativistic correction terms in the equations of hydrodynamics. Similarly large differences as for the phase
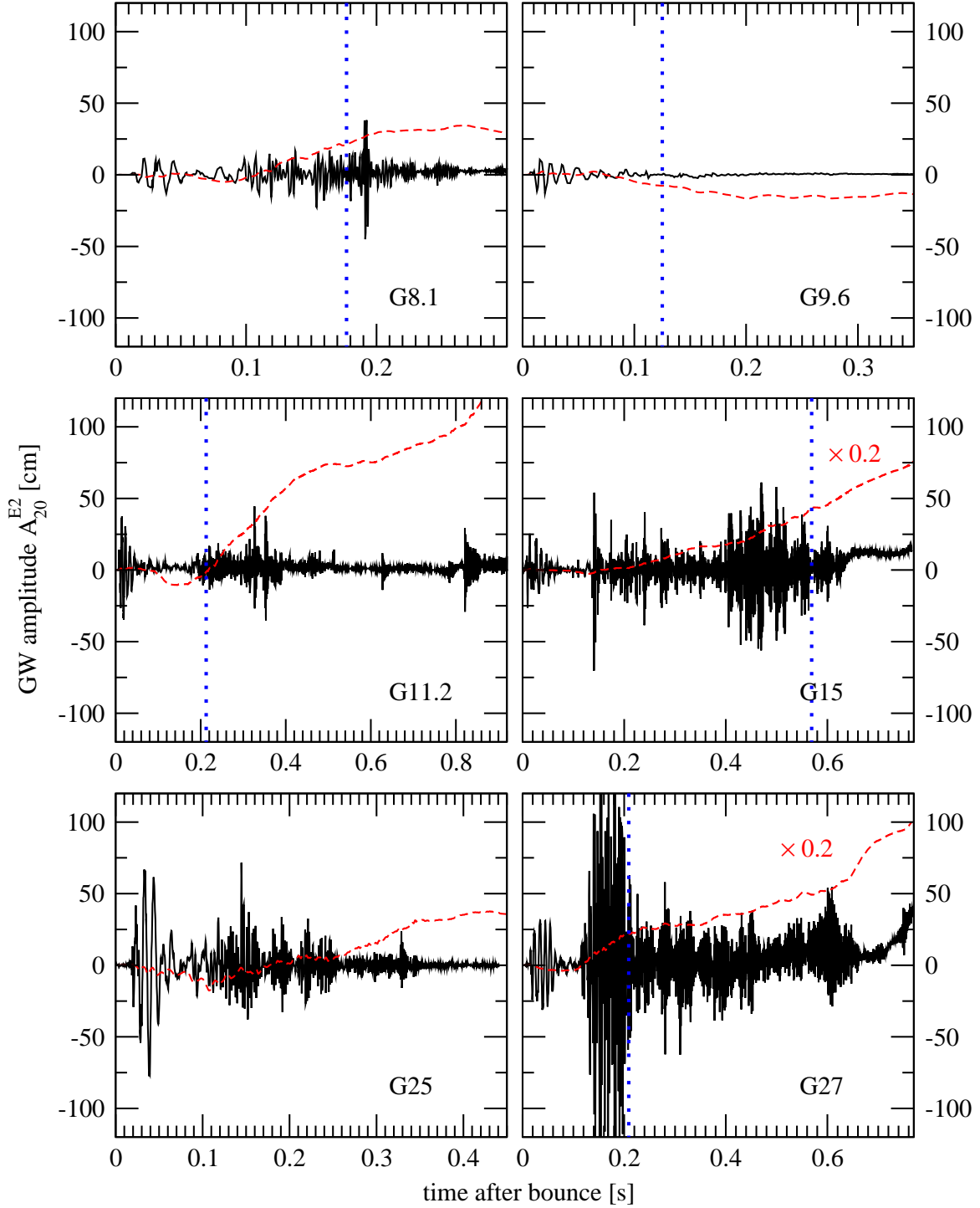
Figure 15. Matter and neutrino gravitational wave amplitudes A_{20}^{E2} from GR simulations of the six progenitors considered in this paper. The matter and neutrino signals are shown as solid black and dashed red curves, respectively. For models G15 and G27, the gravitational wave signal from the anisotropic emission of neutrinos has been rescaled by a factor of 0.2. For the exploding models, the onset of the explosion (defined as the time when the average shock radius reaches 400 km) is indicated by a dotted blue line.
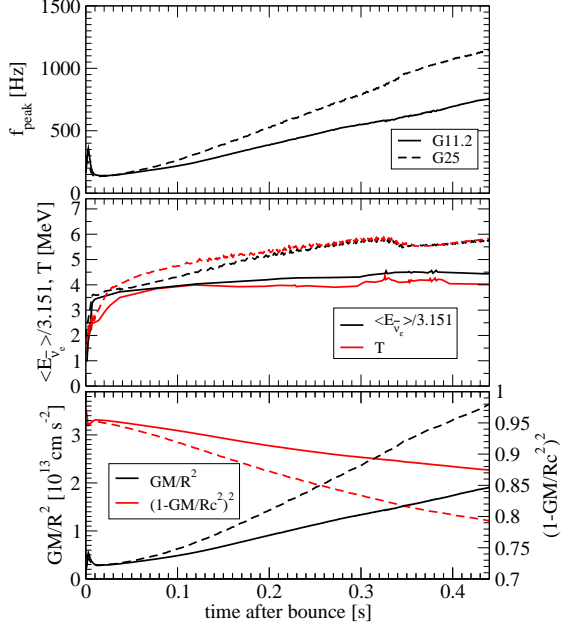
Figure 16. Comparison of the terms contributing to the gravitational wave peak frequency f_{peak} in Equation (17) for models G11.2 (solid lines) and G25 (dashed lines). The proto-neutron star surface temperature T and the temperature $\langle E_{\bar{\nu}_e}/3.151\rangle$ corresponding to the mean electron antineutrino energy (assuming a Fermi distribution with vanishing chemical potential) are shown in the middle panel. The estimated neutron star surface gravity GM/R^2 and the the relativistic correction factor $(1 - GM/Rc^2)^2$ in Equation (17) are shown in the bottom panel, and the resulting estimate for the peak frequency is depicted in the top panel. Note that we define the neutron star surface by a fiducial density of 10^{11} g cm^{-3}.

of hot-bubble convection were also seen for the quasi-periodic signal produced by prompt convection and early SASI activity.

Apart from systematic GR effects, we observed novel features in the GW signal during the explosion phase for the $11.2 M_\odot$ progenitor, a model that is likely to represents a fallback supernova. Here the fallback of material onto the proto-neutron star through newly-forming downflows in the explosion phase leads to a strong excitation of surface g-mode oscillations, which produce burst-like GW signals that are sharply defined in frequency space. These late-time bursts are correlated with small bursts of enhanced ν_e and $\bar{\nu}_e$ emission. Contrary to what more energetic explosion models (Murphy et al. 2009; Yakunin et al. 2010) might suggest, strong GW emission in the high-frequency band late in the explosion phase appears to be possible for underenergetic supernovae. In all other respects, however, our models qualitatively confirm the four-phase picture of gravitational emission with an early quasi-periodic signal, a quiescent phase of several tens of milliseconds, a strong stochastic GW signal lasting until some fraction of a second after the onset of the explosion, and a low-frequency tail-signal from anisotropic neutrino emission and shock expansion.

Our simulations also revealed trends for the progenitor dependence of the GW signal. We found a variation of the maximum signal amplitude by more than an order of magnitude between our two extreme cases with $9.6 M_\odot$ and $27 M_\odot$. In general, high mass accretion rates turn out to be conducive to strong GW activity provided

that an explosion still develops. The time-dependent dominant emission frequency varies by $\sim 30\%$ with a tendency towards higher values for more massive proto-neutron stars. The explosion dynamics plays a major role for determining the time-integrated spectrum, which is therefore more difficult to relate to PNS properties.

While the GW signal predictions presented here rely on state-of-the-art 2D supernova simulations with sophisticated neutrino transport, further research into the gravitational wave signals clearly remains a priority in core-collapse supernova studies. Model uncertainties, e.g. concerning the nuclear equation of state, the progenitor structure, or the role of 3D effects, need to be eliminated in order to predict precise amplitudes and frequencies for specific stellar progenitors. In particular, 3D modeling will be essential for determining the correct signal amplitudes for both the plus and cross polarization modes (the latter of which is not present in our models due to the assumption of axisymmetry) simply because the energy contained in aspherical motions will be distributed differently among more available modes than in 2D. If 3D effects change the overall dynamics of the accretion and explosion phase considerably, e.g. by allowing faster and more energetic explosions, this will also have a direct impact on the GW emission and may modify the details of the progenitor dependence. However, the present controversy about the role of 3D effects (Nordhaus et al. 2010; Hanke et al. 2012; Burrows et al. 2012; Murphy et al. 2012; Dolence et al. 2012; Couch 2012; Takiwaki et al. 2012; see Janka et al. 2012 for an overview discussion) precludes any premature statement. Different from the case of the GW amplitudes, we do not expect that 3D effects will change the frequency structure of the GW signal considerably.

At any rate, our findings clearly demonstrate that a proper treatment of GR is indispensable for obtaining accurate predictions of gravitational waveforms and spectra. In particular, GR simulations will be required to link the GW signal to the properties of the nuclear equation of state, or of the progenitor. However, as a cautionary remark, we emphasize that the inclusion of GR effects at the expense of detailed multi-group neutrino transport may potentially yield little gain in our opinion. Although the simplifications of the neutrino rates considered as test case in this paper cause a significant difference only for the early quasi-periodic signal, more radical approximations in the neutrino transport sector may significantly affect the contraction, the compactness, and the surface stratification of the neutron star, and might thus severely alter the GW spectra. For quantitative predictions of GW signals, future 3D simulations of core-collapse supernovae will thus have to include both GR (cf. Kuroda et al. 2012) and reliable neutrino transport.

REFERENCES

Abdikamalov, E. B., Ott, C. D., Rezzolla, L., Dessart, L., Dimmelmeier, H., Marek, A., & Janka, H.-T. 2010, Phys. Rev. D, 81, 044012

Aerts, C., Christensen-Dalsgaard, J., & Kurtz, D. W. 2010, Asteroseismology (Berlin: Springer)

Banyuls, F., Font, J. A., Ibanez, J. M. A., Martí, J. M. A., & Miralles, J. A. 1997, ApJ, 476, 221

Baron, E., Myra, E. S., Cooperstein, J., & van den Horn, L. J. 1989, ApJ, 339, 978

Bethe, H. A. 1990, Rev. Mod. Phys., 62, 801

Blanchet, L., Damour, T., & Schaefer, G. 1990, MNRAS, 242, 289

Blondin, J. M., & Mezzacappa, A. 2006, ApJ, 642, 401

Blondin, J. M., Mezzacappa, A., & DeMarino, C. 2003, ApJ, 584, 971

Brandt, T. D., Burrows, A., Ott, C. D., & Livne, E. 2011, ApJ, 728, 8

Bruenn, S. W. 1985, ApJS, 58, 771

Bruenn, S. W., De Nisco, K. R., & Mezzacappa, A. 2001, ApJ, 560, 326

Buras, R., Rampp, M., Janka, H.-T., & Kifonidis, K. 2006, A&A, 447, 1049

Burrows, A. 2012, ArXiv e-prints

Burrows, A., Dolence, J. C., & Murphy, J. W. 2012, ApJ, 759, 5

Burrows, A., Hayes, J., & Fryxell, B. A. 1995, ApJ, 450, 830

Cordero-Carrión, I., Cerdá-Durán, P., Dimmelmeier, H., Jaramillo, J. L., Novak, J., & Gourgoulhon, E. 2009, Phys. Rev. D, 79, 024017

Cordero-Carrión, I., Cerdá-Durán, P., & Ibáñez, J. M. 2012, Phys. Rev. D, 85, 044023

Couch, S. M. 2012, ArXiv e-prints

Demorest, P. B., Pennucci, T., Ransom, S. M., Roberts, M. S. E., & Hessels, J. W. T. 2010, Nature, 467, 1081

Dimmelmeier, H., Font, J. A., & Müller, E. 2002a, A&A, 388, 917

—. 2002b, A&A, 393, 523

Dimmelmeier, H., Novak, J., Font, J. A., Ibáñez, J. M., & Müller, E. 2005, Phys. Rev. D, 71, 064023:1

Dimmelmeier, H., Ott, C. D., Janka, H.-T., Marek, A., & Müller, E. 2007a, Phys. Rev. Lett., 98, 251101:1

Dimmelmeier, H., Ott, C. D., Janka, H.-T., Marek, A., & Müller, E. 2007b, in 42nd Rencontres de Moriond, Gravitational Waves and Experimental Gravity, La Thuile, Italy, 2007, ed. J. Dumarchez & J. Tran Thanh Van (Vietnam: The Giói Publishers), 59

Dimmelmeier, H., Ott, C. D., Marek, A., & Janka, H.-T. 2008, Phys. Rev. D, 78, 064056:1

Dolence, J. C., Burrows, A., Murphy, J. W., & Nordhaus, J. 2012, ArXiv e-prints

Einstein, A. 1918, Sitzungsberichte der Königlich Preußischen Akademie der Wissenschaften (Berlin), Seite 154-167, 154

Epstein, R. 1978, ApJ, 223, 1037

Epstein, R. I. 1979, MNRAS, 188, 305

Fernández, R. 2010, ApJ, 725, 1563

Fernández, R., & Thompson, C. 2009, ApJ, 703, 1464

Finn, L. S. 1989, in Frontiers in Numerical Relativity, ed. C. R. Evans, L. S. Finn, & D. W. Hobill (Cambridge (UK): Cambridge University Press), 126–145

Finn, L. S., & Evans, C. R. 1990, ApJ, 351, 588

Foglizzo, T., Galletti, P., Scheck, L., & Janka, H.-T. 2007, ApJ, 654, 1006

Foglizzo, T., Scheck, L., & Janka, H.-T. 2006, ApJ, 652, 1436

Fryer, C. L., Holz, D. E., & Hughes, S. A. 2004, ApJ, 609, 288

Fuller, G. M., Fowler, W. A., & Newman, M. J. 1982, ApJS, 48, 279

Hanke, F., Marek, A., Müller, B., & Janka, H.-T. 2012, ApJ, 755, 138

Heger, A., Woosley, S. E., & Spruit, H. C. 2005, ApJ, 626, 350

Herant, M., Benz, W., & Colgate, S. 1992, ApJ, 395, 642

Herant, M., Benz, W., Hix, W. R., Fryer, C. L., & Colgate, S. A. 1994, ApJ, 435, 339

Hillebrandt, W., & Wolff, R. G. 1985, in Nucleosynthesis: Challenges and New Developments, ed. W. D. Arnett & J. W. Truran, 131

Iwakami, W., Kotake, K., Ohnishi, N., Yamada, S., & Sawada, K. 2008, ApJ, 678, 1207

—. 2009, ApJ, 700, 232

Janka, H.-T. 2012, Annual Review of Nuclear and Particle Science, 62, 407

Janka, H.-T., Hanke, F., Huedepohl, L., Marek, A., Mueller, B., & Obergaulinger, M. 2012, ArXiv e-prints

Janka, H.-T., & Müller, E. 1996, A&A, 306, 167

Kippenhahn, R., & Weigert, A. 1990, Stellar Structure and Evolution (Berlin: Springer)

Kotake, K., Iwakami, W., Ohnishi, N., & Yamada, S. 2009, ApJ, 697, L133

Kotake, K., Ohnishi, N., & Yamada, S. 2007, ApJ, 655, 406

Kotake, K., Sumiyoshi, K., Yamada, S., Takiwaki, T., Kuroda, T., Suwa, Y., & Nagakura, H. 2012, Progress of Theoretical and Experimental Physics, 2012, 301

Kuroda, T., Kotake, K., & Takiwaki, T. 2012, ApJ, 755, 11

Lattimer, J. M., & Swesty, F. D. 1991, Nucl. Phys. A, 535, 331

Lentz, E. J., Mezzacappa, A., Bronson Messer, O. E., Liebendörfer, M., Hix, W. R., & Bruenn, S. W. 2012, ApJ, 747, 73

Liebendörfer, M. 2005, ApJ, 633, 1042

Marek, A., Dimmelmeier, H., Janka, H.-T., Müller, E., & Buras, R. 2006, A&A, 445, 273

Marek, A., Janka, H., & Müller, E. 2009, A&A, 496, 475

Mathews, J. 1962, ApJ, 10, 768

Müller, B., Janka, H., & Dimmelmeier, H. 2010, ApJS, 189, 104

Müller, B., Janka, H.-T., & Heger, A. 2012a, ArXiv e-prints

Müller, B., Janka, H.-T., & Marek, A. 2012b, ApJ, 756, 84

Müller, E. 1998, in Saas-Fee Advanced Course 27: Computational Methods for Astrophysical Fluid Flow. (Berlin: Springer), 343–494

Müller, E., & Janka, H.-T. 1997, A&A, 317, 140

Müller, E., Janka, H.-T., & Wongwathanarat, A. 2012c, A&A, 537, A63

Müller, E., Rampp, M., Buras, R., Janka, H.-T., & Shoemaker, D. H. 2004, ApJ, 603, 221

Murphy, J. W., Dolence, J. C., & Burrows, A. 2012, ArXiv e-prints

Murphy, J. W., Ott, C. D., & Burrows, A. 2009, ApJ, 707, 1173

Nagar, A., Zanotti, O., Font, J. A., & Rezzolla, L. 2007, Phys. Rev. D, 75, 044016:1

Nakamura, T., & Oohara, K. 1989, Methods in 3 D numerical relativity, ed. Evans, C. R., Finn, L. S., & Hobill, D. W. (Cambridge University Press), 254–280

Nordhaus, J., Burrows, A., Almgren, A., & Bell, J. 2010, ApJ, 720, 694

Ohnishi, N., Kotake, K., & Yamada, S. 2006, ApJ, 641, 1018

Ott, C. D. 2009, Classical and Quantum Gravity, 26, 063001

Ott, C. D., Burrows, A., Dessart, L., & Livne, E. 2006, Physical Review Letters, 96, 201102

—. 2008, ApJ, 685, 1069

Ott, C. D., Dimmelmeier, H., Marek, A., Janka, H.-T., Hawke, I., Zink, B., & Schnetter, E. 2007a, Phys. Rev. Lett., 98, 261101:1

Ott, C. D., Dimmelmeier, H., Marek, A., Janka, H.-T., Zink, B., Hawke, I., & Schnetter, E. 2007b, Class. Quantum Grav., 24, S139

Ott, C. D., et al. 2012, Phys. Rev. D, 86, 024026

Pati, M. E., & Will, C. M. 2000, Phys. Rev. D, 62, 124015

Rampp, M., & Janka, H.-T. 2002, A&A, 396, 361

Scheck, L., Janka, H.-T., Foglizzo, T., & Kifonidis, K. 2008, A&A, 477, 931

Scheidegger, S., Whitehouse, S. C., Käppeli, R., & Liebendörfer, M. 2010, Classical and Quantum Gravity, 27, 114101

Shen, H., Toki, H., Oyamatsu, K., & Sumiyoshi, K. 1998, Nucl. Phys. A, 637, 435

Shibata, M., & Sekiguchi, Y.-I. 2003, Phys. Rev. D, 68, 104020:1

Straumann, N. 2004, General Relativity with Applications to Astrophysics (Berlin: Springer)

Suwa, Y., Takiwaki, T., Kotake, K., Fischer, T., Liebendoerfer, M., & Sato, K. 2012, ArXiv Astrophysics e-prints, 1206.6101

Swesty, F. D., Lattimer, J. M., & Myra, E. S. 1994, ApJ, 425, 195

Takiwaki, T., Kotake, K., & Suwa, Y. 2012, ApJ, 749, 98

Thompson, T. A., Burrows, A., & Pinto, P. A. 2003, ApJ, 592, 434

Thorne, K. S. 1966, ApJ, 144, 201

—. 1980, Reviews of Modern Physics, 52, 299

Torrence, C., & Compo, G. P. 1998, Bulletin of the American Meteorological Society, 79, 61

Weber, J. 1966, Physical Review Letters, 17, 1228

Woosley, S. E., Heger, A., & Weaver, T. A. 2002, Rev. Mod. Phys., 74, 1015

Woosley, S. E., & Weaver, T. A. 1995, ApJS, 101, 181

Yakunin, K. N., et al. 2010, Classical and Quantum Gravity, 27, 194005

Zerilli, F. J. 1970, Journal of Mathematical Physics, 11, 2203

APPENDIX

A. GRAVITATIONAL WAVE EXTRACTION: THE MATTER SIGNAL

Although the standard Newtonian quadrupole formula for the matter signal and its time-integrated varieties (Finn 1989; Finn & Evans 1990; Blanchet et al. 1990) as used in the CoCoNuT code so far (Dimmelmeier et al. 2002b, 2008) has proved reasonably accurate (i.e. on a level of $10\% \ldots 20\%$) even for relatively strong gravitational fields in comparison with more sophisticated direct wave extraction methods (Shibata & Sekiguchi 2003; Nagar et al. 2007), it suffers from several drawbacks: Its application in the context of general relativistic hydrodynamics simulation is beset with a number of ambiguities concerning the proper generalization of the source density ρ. Moreover, the transformation of the second time derivative of the mass quadrupole moment to a numerically more tractable form (time-integrated quadrupole formula, stress formula) that does not introduce excessive numerical noise becomes less straightforward than in the Newtonian limit. These problems can give rise to certain pathologies in the computed gravitational wave signals such as spurious offsets (cp. Appendix A in Dimmelmeier et al. 2002b), most notably (but not exclusively) with the Newtonian stress formula.

Evolving the full space-time metric and using direct extraction would be an obvious solution to the problem, but this would not only require that we sacrifice the stable xCFC formulation of the metric, but introduce other difficulties as well: Direct extraction methods can be expected to be very vulnerable to numerical noise as the gravitational wave signal from core-collapse supernovae is weak in the sense that it carries away only a minuscule fraction of the total mass of the system. Post-Newtonian generalizations of the quadrupole formula (Blanchet et al. 1990) provide another possible workaround, but tend to be considerably more cumbersome than the standard quadrupole formula. For the extraction of gravitational waves from our core-collapse supernova simulations, we prefer a somewhat simpler solution that still meets the following requirements:

- No higher time derivatives are required for extracting the wave signal.

- The gravitational wave amplitude vanishes for a stationary flow.

- The generalization of the quadrupole formula should (and need only) be valid for the conditions typically encountered in core-collapse supernova simulations.

Due to the restriction to the supernova context, several approximations can be made: Concerning the matter sources, we assume all velocities to be sufficiently small to disregard retardation effects. Concerning the space-time metric, we consider only small perturbations on the background of a CFC metric $g_{\mu\nu}$, which is given in terms of the lapse function α, the shift vector β^i, the conformal factor ϕ, and the flat-space three metric $\tilde{\gamma}_{ij}$ as

$$g_{\mu\nu} = \begin{pmatrix} -\alpha^2 + \beta_i\beta^i & \beta^i \\ \beta^i & \phi^4\tilde{\gamma}^{ij} \end{pmatrix}. \tag{A1}$$

For deriving our modified quadrupole formula, we use Cartesian spatial coordinates so that $\tilde{\gamma}^{ij} = \delta^{ij}$, and only convert to spherical polar coordinates to obtain the final formulae (Equations A14 and A16). We also assume that the space-time is almost stationary with vanishing shift,

$$\frac{\partial\alpha}{\partial t} \approx 0, \quad \frac{\partial\phi}{\partial t} \approx 0, \quad \beta^i \approx 0. \tag{A2}$$

Furthermore, we observe empirically that for the typical field strength reached in the proto-neutron star environment, the lapse function and the conformal factor obey the relation

$$\alpha\phi^2 \approx 1, \tag{A3}$$

which is a direct consequence of the fact that the field strength is moderate and that the Eulerian energy density E is the dominating source term in both the non-linear Poisson equations for $\alpha\phi$ and ϕ (cp. paper I).

With these approximations for the space-time metric, it can easily be verified that the harmonic gauge condition $\partial/\partial x^\nu(\sqrt{-g}g^{\mu\nu}) = 0$ is satisfied. We can therefore use the relaxed field equations (Straumann 2004; Pati & Will 2000) to compute gravitational amplitudes perturbatively on the background of the CFC metric. The relaxed field equations in geometrized units read

$$\Box\tilde{g}^{\mu\nu} = 16\pi G(-g)\left(T^{\mu\nu} + \tau_{\mathrm{LL}}^{\mu\nu}\right) + \mathcal{D}(\tilde{g}^{\mu\nu}), \tag{A4}$$

with $g = \det(g_{\mu\nu})$, $\tilde{g}^{\mu\nu} = (-g)g^{\mu\nu}$. Here, $T^{\mu\nu}$ and $\tau_{\mathrm{LL}}^{\mu\nu}$ are the stress-energy tensor of the matter and the Landau-Lifschitz pseudo-tensor for the gravitational field, respectively, and $\mathcal{D}$ is a non-linear differential operator. For our derivation of a modified quadrupole formula, it is convenient to follow Straumann (2004) and to introduce $h^{\mu\nu} = \eta^{\mu\nu} - \sqrt{-g}g^{\mu\nu}$ (where $\eta^{\mu\nu}$ is the flat-space Minkowski metric).

The relaxed field equations are amenable to an iterative solution by means of the Green's function method, i.e. solutions for $h^{\alpha\beta}$ can be obtained (Straumann 2004) by successively computing

$$h^{\mu\nu}(t, \mathbf{x}) = 4 \int \frac{\tau^{\mu\nu}(t' = t - |\mathbf{x} - \mathbf{x}'|, \mathbf{x}')}{|\mathbf{x} - \mathbf{x}'|} \mathrm{d}^3x', \tag{A5}$$

and updating the source $\tau^{\mu\nu} = (-g)(T^{\mu\nu} + \tau_{\mathrm{LL}}^{\mu\nu}) + \mathcal{D}(\tilde{g}^{\mu\nu})/(16\pi G)$ in the process. In general, this procedure is beset with a number of difficulties (such as the treatment of non-compact sources and the occurrence of divergences in higher-order approximations), but it can readily be used to obtain an estimate for the gravitational wave amplitude for the matter signal in our case: As in the usual derivation of the Newtonian quadrupole formula, we assume that the source is small compared to the wavelength and that retardation effects can be neglected, in which case Equation (A5) can be written as[5]

$$h^{\mu\nu}(t, \mathbf{x}) \approx \frac{4}{|\mathbf{x}|} \int \tau^{\mu\nu}(t' = t - |\mathbf{x}|, \mathbf{x}') \, \mathrm{d}^3 x'. \tag{A6}$$

By projecting $h^{\mu\nu}$ onto the subspace of symmetric transverse-traceless (STT) tensors, one obtains the angle-dependent gravitational wave amplitude, which can then be decomposed into pure-spin tensor harmonics (Mathews 1962; Zerilli 1970; Thorne 1980) of degree $\ell = 2$. These are already completely determined by the purely spatial components h^{ij}.

At this point, the complicated metric-dependent terms in $\tau^{\mu\nu}$ are the major obstacle for formulating a simple integral expression for the gravitational wave amplitude. However, using the fact that $\tau^{\mu\nu}$ is divergence-free ($\partial_\nu \tau^{\mu\nu} = 0$), the integral in Equation (A6) can be transformed into an integral over τ^{0j} or τ^{00} at the cost of introducing time derivatives:

$$h^{ij}(t, \mathbf{x}) = \frac{4}{|\mathbf{x}|} \frac{\partial}{\partial t} \int x^i \tau^{0j}(t - |\mathbf{x}|, \mathbf{x}') \, \mathrm{d}^3 x' = \frac{4}{|\mathbf{x}|} \frac{\partial^2}{\partial t^2} \int x^i x^j \tau^{00}(t - |\mathbf{x}|, \mathbf{x}') \, \mathrm{d}^3 x'. \tag{A7}$$

The formula for h^{ij} containing the time derivative of τ^{0j} is particularly useful because it does not contain purely gravitational contributions due to our assumptions for the metric functions, and can therefore be expressed in terms of the covariant Eulerian three-momentum density $S_j = \rho h W^2 v_j$ (with h and W being the relativistic specfcic enthalpy including rest mass contributions and the Lorenz factor, respectively) as

$$\tau^{0j} = (-g)T^{0j} = \alpha^2 \phi^{12}(\alpha^{-1}\phi^{-4}S_j) = \alpha\phi^8 S_j = \phi^6 S_j = \sqrt{\gamma}S_j, \tag{A8}$$

which is exactly the conserved quantity in our formulation of the equations of hydrodynamics (Banyuls et al. 1997). The reader should note that our assumption of a diagonal space-time metric and Cartesian spatial coordinates allows us to raise and lower indices simply by multiplying with a scalar factor. We repeatedly and implicitly make uses of this in the following equations. Plugging in the expression for $\partial\sqrt{\gamma}S_j/\partial t$ (cp. also Equation C1), we now obtain

$$h^{ij}(t, \mathbf{x}) = \frac{4}{|\mathbf{x}|} \int x^i \left(\frac{\partial\sqrt{\gamma}S_j}{\partial t} \right)_{\mathrm{hyd}} (t - |\mathbf{x}|, \mathbf{x}') \, \mathrm{d}^3 x' = \frac{4}{|\mathbf{x}|} \int x^i \left[\frac{\sqrt{-g}}{2} T^{\mu\nu} \frac{\partial g_{\mu\nu}}{\partial x^j} - \frac{\partial\sqrt{-g}\left(S_j \hat{v}^k + P\delta_j^k\right)}{\partial x^k} \right] (t - |\mathbf{x}|, \mathbf{x}') \, \mathrm{d}^3 x'. \tag{A9}$$

Here, P is the pressure, and $\hat{v}^i = v^i - \alpha^{-1}\beta^i \approx v^i$ (according to our assumption of a negligible shift vector). Note that the time derivative of $\sqrt{\gamma}S_j$ includes only the (hydrodynamical) changes due to advection, pressure gradients and gravitational source terms, *but no neutrino momentum source term* $\sqrt{\gamma}\dot{S}_{j,\nu}$:

$$\left(\frac{\partial\sqrt{\gamma}S_j}{\partial t} \right)_{\mathrm{hyd}} = \frac{\partial\sqrt{\gamma}S_j}{\partial t} - \sqrt{\gamma}\dot{S}_{j,\nu}. \tag{A10}$$

As $\sqrt{\gamma}\dot{S}_{j,\nu}$ is exactly balanced by a source term for the neutrino energy-momentum tensor, momentum exchange between the matter and the neutrinos does not contribute as a source for gravitational waves.

While formula (A9) for h^{ij} is already amenable to a numerical treatment (no time derivatives are required), it can be cast into a form corresponding more closely to the Newtonian stress formula. Using partial integration, the term containing the flux divergence can be eliminated again,

$$h^{ij}(\mathbf{x}) = \frac{4}{|\mathbf{x}|} \left[\int x^i \frac{\sqrt{-g}}{2} T^{\mu\nu} \frac{\partial g_{\mu\nu}}{\partial x^j} + \sqrt{-g}\left(S_j \hat{v}^i + P\delta_j^i \right) \mathrm{d}^3 x' \right], \tag{A11}$$

where we have suppressed the arguments t and t' for the sake of simplicity. Upon extracting the symmetric transverse-tracefree (STT) part of the right-hand side, the pressure term drops out,

$$h_{\mathrm{TT}}^{ij}(\mathbf{x}) = \frac{4}{|\mathbf{x}|} \left(\int x^i \frac{\sqrt{-g}}{2} T^{\mu\nu} \frac{\partial g_{\mu\nu}}{\partial x^j} + \sqrt{-g}S_j \hat{v}^i \, \mathrm{d}^3 x'. \right)_{\mathrm{STT}}. \tag{A12}$$

The resemblance to the Newtonian stress formula, (Nakamura & Oohara 1989; Blanchet et al. 1990)

$$h_{\mathrm{TT}}^{ij}(\mathbf{x}) = \frac{4}{|\mathbf{x}|} \left(\int -x^i \rho \frac{\partial\Phi}{\partial x_j} + \rho v_j v^i \, \mathrm{d}^3 x', \right)_{\mathrm{STT}} \tag{A13}$$

is evident. The decomposition of the gravitational radiation field given by Equation (A12) into pure-spin harmonics proceeds exactly as in the Newtonian case. In the case of axisymmetry, only the "electric" quadrupole with $m = 0$ is

---

[5] We emphasize that unlike Equation (A5), Equation (A6) can no longer be used to compute the gravitational wave signal due to anisotropic neutrino emission, which must include retardation effects as neutrinos propagate with the same velocity as the gravitational waves themselves.

present, and its amplitude A_{20}^{E2} can be expressed in spherical polar coordinates as,

$$A_{20}^{\mathrm{E2}} = \frac{32\pi^{3/2}}{\sqrt{15}} \iint \alpha\phi^6 r^2 \sin\theta \left[S_r \hat{v}^r \left(3\cos^2\theta - 1 \right) + S_\theta \hat{v}^\theta \left(2 - 3\cos^2\theta \right) - S_\varphi \hat{v}^\varphi - 6rS_r \hat{v}^\theta \sin\theta\cos\theta \right.$$
$$\left. - \dot{S}_{r,\mathrm{grav}} r \left(3\cos^2\theta - 1 \right) + 3\dot{S}_{\theta,\mathrm{grav}} r \sin\theta\cos\theta \right] \, \mathrm{d}\theta \, \mathrm{d}r, \tag{A14}$$

where $\dot{S}$ designates the gravitational source term in the momentum equation:

$$\dot{S}_{i,\mathrm{grav}} = \frac{1}{2} T^{\mu\nu} \frac{\partial g_{\mu\nu}}{\partial x^i}. \tag{A15}$$

Alternatively, one can retain the time-derivative $\partial\sqrt{\gamma}S_j/\partial t$ in Equation (A9) and formulate a modified version of the time-integrated quadrupole formula, but the neutrino momentum source term needs to be handled with care in this case. In order to avoid double counting, these source terms must be subtracted from the time derivative of $\sqrt{\gamma}S_j$, and we therefore obtain (after converting to spherical polar coordinates again)

$$A_{20}^{\mathrm{E2}} = \frac{32\pi^{3/2}}{\sqrt{15}} \frac{\partial}{\partial t} \iint \phi^6 r^3 \sin\theta \left[S_r \left(3\cos^2\theta - 1 \right) + 3r^{-1} S_\theta \sin\theta\cos\theta \right] \, \mathrm{d}\theta \, \mathrm{d}r$$
$$- \frac{32\pi^{3/2}}{\sqrt{15}} \iint \phi^6 r^3 \sin\theta \left[\dot{S}_{r,\nu}, \left(3\cos^2\theta - 1 \right) + 3r^{-1}\dot{S}_{\theta,\nu} \sin\theta\cos\theta \right] \, \mathrm{d}\theta \, \mathrm{d}r. \tag{A16}$$

Since our modified stress formula has been obtained through *exact* transformations of Equation (A11), which contains the time derivative of S_j under the integral, it does not produce any unphysical offset in the gravitational wave signal for stationary configurations with $\partial S_j/\partial t = 0$ in the limit of infinite spatial resolution.[6] It also avoids the contamination of the matter signal by neutrino momentum source terms since it allows for a nice separation of the source density for the wave equation into terms due to the hydrodynamic momentum flux and gravitational source terms. However, the contribution from neutrino stresses is small in practice, and may even be neglected in Equation (A11) with little loss of accuracy.

B. GRAVITATIONAL WAVE SIGNAL FROM ASPHERICAL SHOCK PROPAGATION

As mentioned in Section 4, it is possible to formulate a simple analytic expression for the contribution of asymmetric shock propagation to the gravitational wave signal in the limit of a relatively small deformation of the shock. To this end, we perform the integral in the quadrupole formula (A16) over a narrow region around the shock between $r_a(\theta)$ and $r_b(\theta)$ in radius such as to neglect slower, secular variations in the pre- and post-shock conditions. For the sake of simplicity, we disregard relativistic kinematics and strong-field effects, setting $\alpha = \phi = 1$ and $S_i = \rho v_i$ for the momentum density. As we confine ourselves to a weakly deformed shock, we also neglect the non-radial component v_θ of the post-shock velocity[7] and obtain the contribution of the shock to $A_{20,\mathrm{shock}}^{\mathrm{E2}}$ in terms of the (angle-dependent) shock radius $r_{\mathrm{sh}}(\theta)$, and the radial pre- and post-shock velocities $(v_{\mathrm{r,p}}, v_{\mathrm{r,s}})$ and densities $(\rho_{\mathrm{p}}, \rho_{\mathrm{s}})$,

$$A_{20,\mathrm{shock}}^{\mathrm{E2}} \approx \frac{32\pi^{3/2}}{\sqrt{15}} \frac{\mathrm{d}}{\mathrm{d}t} \int_0^\pi \sin\theta \left[\int_{r_a}^{r_{\mathrm{sh}}(\theta)} r^3 \rho v_r (3\cos^2\theta - 1) \, \mathrm{d}r + \int_{r_{\mathrm{sh}}(\theta)}^{r_b} r^3 \rho v_r (3\cos^2\theta - 1) \, \mathrm{d}r \right] \, \mathrm{d}\theta$$
$$= \frac{32\pi^{3/2}}{\sqrt{15}} \frac{\mathrm{d}}{\mathrm{d}t} \int_0^\pi r_{\mathrm{sh}}^3(\theta) \sin\theta (3\cos^2\theta - 1) \left(\rho_{\mathrm{s}} v_{\mathrm{r,s}} - \rho_{\mathrm{p}} v_{\mathrm{r,p}} \right) \, \mathrm{d}\theta. \tag{B1}$$

By exploiting the Rankine-Hugoniot jump conditions, the difference of the post-shock and pre-shock mass flux can be eliminated and the shock velocity v_{sh} appears instead:

$$\rho_{\mathrm{s}} v_{\mathrm{r,s}} - \rho_{\mathrm{p}} v_{\mathrm{r,p}} = \left(\rho_{\mathrm{s}} - \rho_{\mathrm{p}} \right) v_{\mathrm{sh}} = \left(\rho_{\mathrm{s}} - \rho_{\mathrm{p}} \right) \dot{r}_{\mathrm{sh}}. \tag{B2}$$

Thus, we obtain

$$A_{20,\mathrm{shock}}^{\mathrm{E2}} \approx \frac{32\pi^{3/2}}{\sqrt{15}} \frac{\mathrm{d}}{\mathrm{d}t} \int_0^\pi \left(\rho_{\mathrm{s}}(\theta) - \rho_{\mathrm{p}}(\theta) \right) r_{\mathrm{sh}}^3(\theta) \dot{r}_{\mathrm{sh}}^2(\theta) (3\cos^2\theta - 1) \sin\theta \, \mathrm{d}\theta. \tag{B3}$$

$r_{\mathrm{sh}}(\theta)$ can be decomposed into spherical harmonics, or, in the case of axisymmetry, into Legendre polynomials,

$$r_{\mathrm{sh}}(\theta) = \sum_{\ell=0} P_\ell(\cos\theta) a_\ell. \tag{B4}$$

---

[6] For finite resolution, the identity $\int \tau^{ij} \, \mathrm{d}V = \int x^j \tau^{0i} \, \mathrm{d}V = \int \tau^{00} x^i x^j \, \mathrm{d}V$ does not hold exactly due to discretization errors, but in practice the wave signal is hardly affected by this problem.

[7] Non-radial velocities occur behind a non-spherical shock, but a more detailed analysis of the jump conditions for oblique shocks reveals that this leads only to higher-order corrections to the resulting gravitational wave amplitude.

Assuming a power-law dependence of the pre-shock density $\rho \propto r^\gamma$ and a fixed ratio β of the post-shock and pre-shock density, we can express the angle-dependence of $\rho_s(\theta)$ and $\rho_p(\theta)$ in terms of a_ℓ as well:

$$\rho_{\rm s}(\theta) - \rho_{\rm p}(\theta) = (\beta - 1)\bar{\rho}_{\rm p} \left(\frac{r_{\rm sh}(\theta)}{a_0}\right)^\gamma = (\beta - 1)\bar{\rho}_{\rm p} \left[1 + \gamma \sum_{\ell=1} P_\ell(\cos\theta)a_\ell a_0^{-1} + \frac{\gamma(\gamma+1)}{2}\left(\sum_{\ell=1} P_\ell(\cos\theta)a_\ell a_0^{-1}\right)^2 + \ldots\right]. \tag{B5}$$

Here, $\bar{\rho}_{\rm p}$ is an appropriate average value of $\rho_{\rm p}(\theta)$, and the ratio $(r_{\rm sh}(\theta)/a_0)^\gamma$ has been expanded into a power series. The resulting expression for $A_{20,\rm shock}^{\rm E2}$ can be expanded into a power series in the higher multipoles $a_1, a_2, \ldots$ of the shock position. Retaining only the linear terms and converting back to non-geometrized units, we finally obtain:

$$A_{20,\rm shock}^{\rm E2} \approx \frac{256\pi^{3/2}}{5\sqrt{15}}\bar{\rho}_{\rm p}\,(\beta - 1)\,a_0^3\left[(4 + \gamma)\,a_2\dot{a}_0 + \dot{a}_2 a_0\right]. \tag{B6}$$

C. LEDOUX CRITERION, BRUNT-VÄISÄLÄ AND PLUME FREQUENCY IN GENERAL RELATIVITY

It may not be immediately obvious to the reader how buoyancy effects are to be treated in GR, and how, e.g., the analysis of the deceleration of convective downdrafts at the boundary of the convection zone presented by Murphy et al. (2009) carries over to the relativistic case. We therefore briefly recapitulate the principles governing the motion of buoyancy-driven bubbles in the framework of GR hydrodynamics. Although the problem of convective stability has been studied in general relativity (Thorne 1966), we find it advisable to explicitly derive the equations for the particular gauge and frame-of-reference used in our paper in order to eliminate a possible source of confusion.

We start from the relativistic momentum equation in the $3 + 1$ formulation (Banyuls et al. 1997),

$$\frac{\partial\sqrt{\gamma}\rho h W^2 v_i}{\partial t} + \frac{\partial\sqrt{-g}\left[\rho h W^2 v_i\left(v^j - \beta^j/\alpha\right) + \delta_i^j P\right]}{\partial x^j} = \frac{\sqrt{-g}}{2}T^{\mu\nu}\frac{\partial g_{\mu\nu}}{\partial x^j}. \tag{C1}$$

Here, ρ, h, W, P, v_i, $T^{\mu\nu}$ denote the rest-mass density, the specific enthalpy, the Lorentz factor, the pressure, the three-velocity and the stress-energy-tensor of the fluid, respectively. The four-metric $g_{\mu\nu}$ is given in terms of the lapse function α, the shift vector β^i, the conformal factor ϕ, and the flat-space three metric $\tilde{\gamma}_{ij}$ by Equation (A1), which is repeated here for convenience:

$$g_{\mu\nu} = \begin{pmatrix} -\alpha^2 + \beta_i\beta^i & \beta^i \\ \beta^i & \phi^4\tilde{\gamma}^{ij} \end{pmatrix}. \tag{C2}$$

Finally, γ and g denote the determinants of the three-metric γ_{ij} and the four-metric $g_{\mu\nu}$.

We now consider the equation of motion for a convective blob of matter in a hydrostatic background medium which is displaced by a short distance δr from its original position and maintains pressure equilibrium with its surroundings. The acceleration of the blob due to pressure gradients is given by the second term on the LHS of Equation (C1), which can be replaced by the gravitational source term *for the background medium* using the condition of hydrostatic equilibrium. The equation of motion (including the gravitational source term) is therefore given by

$$\left(\frac{\partial\sqrt{\gamma}\rho h W^2 v_i}{\partial t}\right)_{\rm blob} = \frac{\alpha\sqrt{\gamma}}{2}(T_{\rm blob}^{\mu\nu} - T_{\rm bg}^{\mu\nu})\frac{\partial g_{\mu\nu}}{\partial x^j}, \tag{C3}$$

where the subscripts denote whether $T^{\mu\nu}$ is evaluated for the blob or the background medium ("bg"). In order to simplify this result, we assume slow subsonic motion ($v \ll c_s$), and retain density and energy perturbations only in the buoyancy term on the RHS (the Boussinesq approximation). The only remaining contribution on the RHS then contains $T_{\rm blob}^{00} - T_{\rm bg}^{00}$, and we obtain

$$\rho h\frac{{\rm d}v_{\rm r,blob}\phi^2}{{\rm d}t} = -\delta(\rho + \rho\epsilon)\frac{\partial\alpha}{\partial r}, \tag{C4}$$

where $\delta(\rho + \rho\epsilon)$ denotes the (energy-)density contrast between the blob and the background medium (with ϵ denoting the specific internal energy). For a small radial displacement δr from the initial position, $\delta(\rho + \rho\epsilon)$ can be expressed as $C_L\delta r$, C_L being the (relativistic) Ledoux criterion (cp. the "Schwarzschild discriminant" of Thorne 1966),

$$C_{\rm L} = \frac{\partial\rho(1 + \epsilon)}{\partial r} - \left(\frac{{\rm d}\rho(1 + \epsilon)}{{\rm d}P}\right)_{s,Y_e={\rm const.}}\frac{\partial P}{\partial r} = \frac{\partial\rho(1 + \epsilon)}{\partial r} - \frac{1}{c_s^2}\frac{\partial P}{\partial r}. \tag{C5}$$

The equation of motion for the blob can thus be written as

$$\frac{{\rm d}v_{\rm r,blob}}{{\rm d}t} = -\frac{\phi^{-2}C_{\rm L}}{\rho h}\frac{\partial\alpha}{\partial r}\delta r, \tag{C6}$$

or

$$\ddot{r} = \alpha\phi^{-2}\frac{{\rm d}v_{\rm r,blob}}{{\rm d}t} = -\frac{\alpha C_{\rm L}}{\rho h\phi^4}\frac{\partial\alpha}{\partial r}\delta r. \tag{C7}$$

The blob therefore oscillates with an angular frequency N given by

$$N^2 = \frac{\alpha C_{\mathrm{L}}}{\rho h \phi^4} \frac{\partial \alpha}{\partial r}. \tag{C8}$$

This is the relativistic Brunt-Väisälä-frequency. It should be noted that we have measured N in coordinate time and not in the frame of an observer comoving with the fluid. As the spacetime is stationary to very good approximation in our case, this implies that N is also the angular frequency seen by an observer at infinity.[8]

For determining the "plume frequency" and the penetration depth D_p used in the model of Murphy et al. (2009), we estimate the turnaround time T and D_p for a convective blob overshooting into a stable layer assuming a constant value of N equal to that at the turning point during the decelerating process. Moreover, we assume that the initial density contrast to the background medium at the boundary of the convective and non-convective regions is negligible compared to the density contrast after penetration into the non-convective region. Otherwise an additional acceleration term would have to be included in the equation of motion. Equation (C7) can then be solved using $\delta r(0) = 0$ and $\dot{r}(0) = -\alpha\phi^2 v_r$ (v_r being the plume velocity in the convective region) as initial conditions,

$$\delta r(t) = \alpha\phi^2 v_r \sin Nt. \tag{C9}$$

The penetration depth is therefore given by

$$D_p = \alpha\phi^2 v_r, \tag{C10}$$

and the characteristic (ordinary) frequency f_p for the motion of the decelerating blob corresponding to the angular frequency is just

$$f_p = \frac{N}{2\pi}. \tag{C11}$$

---

[8] This can easily be seen by considering geodesics starting from the position of the blob at two different coordinate times t and $t + \delta t$. Because of the stationarity of the metric, the geodesics can be transformed into each other by applying a time translation δt *everywhere*. An observer at infinity therefore measures the same time difference δt.